

# Thermodynamics and phase diagrams of the Polyakov quark-meson model with on-shell versus curvature mass parameter fixing

Suraj Kumar Rai<sup>1,2,\*</sup> and Vivek Kumar Tiwari<sup>1,†</sup>

<sup>1</sup>*Department of Physics, University of Allahabad, Prayagraj 211002, India*

<sup>2</sup>*Department of Physics, Acharya Narendra Deo Kisan P.G. College, Babhnan Gonda 271313, India*

 (Received 24 May 2023; accepted 30 August 2023; published 18 October 2023)

The quantum chromodynamics (QCD) phase structure has been studied using the Polyakov-loop augmented quark-meson model (PQM) in the extended mean field approximation (e-MFA), where the quark one-loop vacuum term is included. When the divergent vacuum term is regularized in the minimal subtraction scheme and the curvature meson masses are used to fix the parameters, the Polyakov quark-meson model with the vacuum term (PQMVT) becomes inconsistent as the curvature masses are determined by calculating the self energies at zero momentum. The above inconsistency is remedied by the on-shell parameter fixing when the pion decay constant and the pole masses of the mesons are put into the relation of the couplings and running mass parameter by using the on-shell and the minimal subtraction renormalization scheme. Combining the modified chiral effective potential of the on-shell renormalized quark-meson model (RQM) with the Polyakov-loop potential that mimics the physics of the confinement-deconfinement transition, we get the renormalized Polyakov quark-meson (RPQM) model. The phase diagrams and the thermodynamics details for the PQM, PQMVT, and RPQM model have been computed and compared for different forms of the Polyakov-loop potentials with and without the quark backreaction. The results have also been compared with the available lattice QCD data. The so-called quarkyonic phase region in the phase diagram, where the chiral symmetry is restored but the quarks and antiquarks are still confined, gets reduced by the quark backreaction in the unquenched Polyakov-loop potential. It altogether disappears for the chemical potential dependent parameter  $T_0 \equiv T_0(\mu)$  in the Log or the PolyLog-gluon form of the Polyakov-loop potential in the RPQM model.

DOI: [10.1103/PhysRevD.108.074014](https://doi.org/10.1103/PhysRevD.108.074014)

## I. INTRODUCTION

The strong interaction theory, quantum chromodynamics (QCD) indicates that under the extreme conditions of high temperatures and/or densities, there should be a phase transition from the normal hadronic matter to a collective form of matter known as the quark gluon plasma (QGP) [1–5]. The general properties of such a hot and dense matter are summarized in the QCD phase diagram [1], which can be probed by the ultrarelativistic heavy ion collision experiments like the RHIC (BNL), LHC (CERN), and the upcoming CBM experiments at the FAIR facility (GSI-Darmstadt). The study of the QCD thermodynamics and its phase structure is a very active area of current

research as several issues are not yet settled. One gets important information and insights regarding the QCD phase transition from the first-principle lattice QCD simulations [6–15], but these calculations get seriously compromised as the QCD action becomes complex due to the fermion sign problem [8] when the baryon density/chemical potential is nonzero. Hence, one turns to the effective models [16–21] for the study of the QCD thermodynamics and its phase diagram.

The QCD Lagrangian has the global  $SU_{L+R}(2) \times SU_{L-R}(2)$  symmetry for the two flavor of massless quarks. In the low energy hadronic vacuum of the QCD, the chiral (axial  $A = L - R$ ) symmetry is spontaneously broken, and one gets the chiral condensate as order parameter and the three massless pions as Goldstone modes. The small explicit breaking of the chiral symmetry due to the light quark masses gives a little mass to the physical pions, which are the lightest among hadrons. The  $SU_L(2) \times SU_R(2)$  linear sigma model [22–24] is a good framework to study the chiral symmetry breaking and restoring phase transition. Coupling the isosinglet  $\sigma$ , isotriplet  $\vec{a}_0$  scalar mesons together with the isosinglet  $\eta$ , isotriplet  $\vec{\pi}$

\*surajrai050@gmail.com

†vivekkrt@gmail.com

Published by the American Physical Society under the terms of the [Creative Commons Attribution 4.0 International license](https://creativecommons.org/licenses/by/4.0/). Further distribution of this work must maintain attribution to the author(s) and the published article's title, journal citation, and DOI. Funded by SCOAP<sup>3</sup>.

pseudoscalar mesons of the sigma model with the two flavor of quarks, one gets the QCD-like framework of the quark-meson (QM) model to study the QCD thermodynamics and its phase diagram in great detail.

The QCD phase structure/phase diagram has already been studied in the chiral models [25–36], and the two and three flavor QM model [37–41]. But the QM model in the standard mean field approximation (s-MFA) gives an inconsistent result as the chiral phase transition at zero baryon densities becomes first-order in the chiral limit, which is at odds with the general theoretical considerations [42,43]. This inconsistency is remedied by the proper treatment of the Dirac sea [44] after including the quark one-loop vacuum fluctuation. In the modified framework of the quark-meson model with the vacuum term (QMVT), several QCD phase structure studies [45–58] regularized the divergent one-loop vacuum term in the minimal subtraction scheme and after identifying the pion decay constant with the vacuum expectation value of the sigma mean field, fixed the model parameters using the curvature masses of the mesons. The above parameter fixing procedure turns out to be inconsistent as one notes that the effective potential is the generator of the  $n$ -point functions of the theory at vanishing external momenta, and the curvature mass is defined by the evaluation of the self-energy at zero momentum [59–63].

The radiative corrections to the physical quantities change their tree level relations to the parameters of the Lagrangian. Hence, the use of tree level values of the parameters for the calculation of effective potential becomes inconsistent. One has to account for the renormalization scale  $\Lambda$  dependence of the running parameters in the (modified) minimal subtraction  $\overline{\text{MS}}$  scheme while the on-shell parameters have their tree-level values. Following the correct renormalization procedure, one needs to calculate the counterterms both in the  $\overline{\text{MS}}$  scheme and in the on-shell scheme and then connect the renormalized parameters of the two schemes. The effective potential is then calculated using the  $\overline{\text{MS}}$  procedure where the relations between the running parameters and the on-shell parameters (physical quantities) are used as input [60]. Using the abovementioned renormalization prescription Adhikari and Collaborators [60,64–66] correctly accounted for the effect of Dirac sea in the QM model whose  $O(4)$  sigma model has the  $\sigma$  and  $\vec{\pi}$  as meson degrees of freedom. In a very recent work [67], we have applied the exact renormalization method for the on-shell parameter fixing to that version of the QM model in which the two flavor of quarks are coupled to the eight mesons (isosinglet and isotriplet combination of the  $\sigma$  and  $\vec{a}_0$  as scalars and the  $\eta$  and  $\vec{\pi}$  as pseudoscalars) of the  $SU_L(2) \times SU_R(2)$  sigma model and termed this setting as the renormalized quark-meson (RQM) model.

The physics of quark confinement in the hadrons at low temperatures and densities is implemented by the

introduction of the Polyakov-loop, where the QCD confinement is mimicked in a statistical sense by coupling the chiral models to a constant background  $SU(N_c)$  gauge field  $A_\mu^a$  [2,68–73]. In such studies, the free energy density from the gluons is added to the QM model using the phenomenological Polyakov-loop potential [74–76], and it becomes the PQM model [77–80]. In the present work, the modified chiral parts of the effective potentials for both the on-shell renormalized quark-meson model (RQM) and the curvature mass parametrized QMVT model have been augmented with the physics of confinement/deconfinement transition by including the Polyakov-loop potential, and the respective settings have been termed as the renormalized Polyakov quark-meson model (RPQM) and the PQMVT model. In this study, we have considered the important improvement of the Polyakov-loop potential from a pure gauge potential to an unquenched glue potential in which backreaction effects of the quarks are included [81–84]. It is worthwhile to explore the consequences of coupling the improved chiral effective potential with the unquenched Polyakov-loop potential because it leads to the linkage of the chiral and deconfinement phase transitions also at small temperatures and large chemical potentials. The abovementioned attribute is also seen in the functional renormalization (FRG) improvement of the PQM model when the Yang-Mills Polyakov-loop potential is used [53,85]. We have computed the relative shift of the critical end point (CEP) and made the qualitative and quantitative comparisons of the phase diagrams and thermodynamics in the RPQM and PQMVT models when different forms of the Polyakov-loop potentials are considered with and without quark backreaction.

The paper is arranged as follows. Section II presents a brief formulation of the  $SU_L(2) \times SU_R(2)$  PQM model. Section II A describes the different forms of the Polyakov-loop potentials, while Sec. II B presents the thermodynamic grand potential in the PQM model. Section III gives a brief account of the Polyakov quark-meson model with the vacuum term (PQMVT). The renormalized Polyakov quark-meson model (RPQM) effective potential has been presented in Sec. IV. Section V gives results and discussion. Section V A discusses the order parameters and their temperature derivatives, Sec. V B describes the sigma mass and the model dependence of the phase diagrams, Sec. V C reports the results for the quarkyonic phase in the RPQM model, Sec. V D explains the computed results for the thermodynamic observables while the specific heat and the speed of sound are discussed in Sec. V E. Section VI presents the summary and conclusion. Appendix A presents the parameter fixing for the QMVT model. The essential steps of the exact on-shell parameter fixing and the calculation of the quark one-loop effective potential in the large  $N_c$  limit for the renormalized quark-meson (RQM) model have been presented in Appendix B. The integrals are presented in Appendix C.

## II. MODEL FORMULATION

We will be combining the Polyakov-loop potential with the  $SU_L(2) \times SU_R(2)$  quark-meson model. In this model, a spatially constant temporal gauge field, two light quarks, and  $SU_V(2) \times SU_A(2)$  symmetric meson fields are coupled together. The Polyakov-loop field  $\Phi$  is defined as the thermal expectation value of color trace of the Wilson loop in temporal direction,

$$\Phi = \frac{1}{N_c} \langle \text{Tr}_c L(\vec{x}) \rangle, \quad \bar{\Phi} = \frac{1}{N_c} \langle \text{Tr}_c L^\dagger(\vec{x}) \rangle, \quad (1)$$

where  $L$  is a matrix in the fundamental representation of the  $SU_c(3)$  color gauge group,

$$L(\vec{x}) = \mathcal{P} \exp \left[ i \int_0^\beta d\tau A_0(\vec{x}, \tau) \right]. \quad (2)$$

Here,  $\mathcal{P}$  is path ordering,  $A_0$  is the temporal component of vector field, and  $\beta = T^{-1}$  [68]. In accordance of Refs. [74,75], we have considered a homogeneous Polyakov-loop field  $\Phi(\vec{x}) = \Phi = \text{constant}$  and  $\bar{\Phi}(\vec{x}) = \bar{\Phi} = \text{constant}$ .

The model Lagrangian has quarks, mesons, couplings, and Polyakov-loop potential  $\mathcal{U}(\Phi, \bar{\Phi}, T)$  as

$$\mathcal{L}_{PQM} = \mathcal{L}_{QM} - \mathcal{U}(\Phi, \bar{\Phi}, T). \quad (3)$$

The Lagrangian of the model [22–24] is written as

$$\begin{aligned} \mathcal{L}_{QM} = & \bar{\psi} [i\gamma^\mu \partial_\mu - g t_0 (\sigma + i\gamma_5 \eta) \\ & - g \vec{t} \cdot (\vec{a} + i\gamma_5 \vec{\pi})] \psi + \mathcal{L}(\mathcal{M}), \end{aligned} \quad (4)$$

where  $\psi$  is a color  $N_c$ -plet, a four-component Dirac spinor, and a flavor doublet,

$$\psi = \begin{pmatrix} u \\ d \end{pmatrix}. \quad (5)$$

The Lagrangian for meson fields is [22]

$$\begin{aligned} \mathcal{L}(\mathcal{M}) = & \text{Tr}(\partial_\mu \mathcal{M}^\dagger \partial^\mu \mathcal{M} - m^2 (\mathcal{M}^\dagger \mathcal{M})) \\ & - \lambda_1 [\text{Tr}(\mathcal{M}^\dagger \mathcal{M})]^2 - \lambda_2 \text{Tr}(\mathcal{M}^\dagger \mathcal{M})^2 \\ & + c [\det \mathcal{M} + \det \mathcal{M}^\dagger] + \text{Tr}[H(\mathcal{M} + \mathcal{M}^\dagger)]; \end{aligned} \quad (6)$$

here, the field  $\mathcal{M}$  is a complex  $2 \times 2$  matrix,

$$\mathcal{M} = t_a \xi_a = t_a (\sigma_a + i\pi_a), \quad (7)$$

$a = 0, 1, 2$ , and  $3$ .  $t_a$  represents the four generators of the  $U(2)$  algebra,

$$\mathcal{M} = t_0 (\sigma + i\eta) + \vec{t} \cdot (\vec{a} + i\vec{\pi}) \quad (8)$$

with  $t_0 = \frac{1}{2} \begin{pmatrix} 1 & 0 \\ 0 & 1 \end{pmatrix}$ ,  $t_1 = \frac{1}{2} \begin{pmatrix} 0 & 1 \\ 1 & 0 \end{pmatrix}$ ,  $t_2 = \frac{1}{2} \begin{pmatrix} 0 & -i \\ i & 0 \end{pmatrix}$ ,  $t_3 = \frac{1}{2} \begin{pmatrix} 1 & 0 \\ 0 & -1 \end{pmatrix}$ .

One can rewrite the Lagrangian (6) in the form [23],

$$\begin{aligned} \mathcal{L}(\mathcal{M}) = & \frac{1}{2} (\partial_\mu \sigma \partial_\mu \sigma + \partial_\mu \vec{\pi} \cdot \partial_\mu \vec{\pi} + \partial_\mu \eta \partial_\mu \eta \\ & + \partial_\mu \vec{a}_0 \cdot \partial_\mu \vec{a}_0) - U, \end{aligned} \quad (9)$$

further,

$$\begin{aligned} U = & \frac{m^2}{2} (\sigma^2 + \vec{\pi}^2 + \eta^2 + \vec{a}^2) - \frac{c}{2} (\sigma^2 - \eta^2 + \vec{\pi}^2 - \vec{a}^2) \\ & + \frac{1}{4} \left( \lambda_1 + \frac{1}{2} \lambda_2 \right) (\sigma^2 + \vec{\pi}^2 + \eta^2 + \vec{a}^2)^2 \\ & + \frac{\lambda_2}{2} ((\sigma^2 + \vec{\pi}^2)(\eta^2 + \vec{a}^2) - (\sigma\eta - \vec{\pi} \cdot \vec{a})^2) - h\sigma. \end{aligned} \quad (10)$$

The  $2 \times 2$  matrix  $H$  explicitly breaks the chiral symmetry and is chosen as

$$H = t_a h_a, \quad (11)$$

where  $h_a$  are external fields. The field  $\sigma$  acquires nonzero vacuum expectation value (VEV),  $\bar{\sigma}$ , due to the spontaneous breaking of the chiral symmetry, while the other scalar and pseudoscalar fields ( $\vec{a}_0, \vec{\pi}, \eta$ ) assume zero VEV. Here, the two parameters  $h_0$  and  $h_3$  may give rise to the explicit breaking of chiral symmetry. We are neglecting the isospin symmetry breaking; hence, we choose  $h_0 \neq 0$  and  $h_3 = 0$ .

The field  $\sigma$  has to be shifted to  $\sigma \rightarrow \bar{\sigma} + \sigma$  as it acquires nonzero VEV. At the tree level, the expression of the meson masses are [22]

$$m_\sigma^2 = m^2 - c + 3 \left( \lambda_1 + \frac{\lambda_2}{2} \right) \bar{\sigma}^2, \quad (12)$$

$$m_{a_0}^2 = m^2 + c + \left( \lambda_1 + \frac{3\lambda_2}{2} \right) \bar{\sigma}^2, \quad (13)$$

$$m_\eta^2 = m^2 + c + \left( \lambda_1 + \frac{\lambda_2}{2} \right) \bar{\sigma}^2, \quad (14)$$

$$m_\pi^2 = m^2 - c + \left( \lambda_1 + \frac{\lambda_2}{2} \right) \bar{\sigma}^2, \quad (15)$$

$$m_q = \frac{g\bar{\sigma}}{2}. \quad (16)$$

Using (12)–(16), the parameters of the Lagrangian (6) are obtained as

$$\lambda_1 = \frac{m_\sigma^2 + m_\eta^2 - m_{a_0}^2 - m_\pi^2}{2f_\pi^2}, \quad (17)$$

$$\lambda_2 = \frac{m_{a_0}^2 - m_\eta^2}{f_\pi^2}, \quad (18)$$

$$m^2 = m_\pi^2 + \frac{m_\eta^2 - m_\sigma^2}{2}, \quad (19)$$

$$c = \frac{m_\eta^2 - m_\pi^2}{2}, \quad (20)$$

$$\frac{g^2}{4} = \frac{m_g^2}{\bar{\sigma}^2}, \quad (21)$$

and the tree level effective potential is written as

$$U(\bar{\sigma}) = \frac{1}{2}(m^2 - c)\bar{\sigma}^2 + \frac{1}{4}\left(\lambda_1 + \frac{1}{2}\lambda_2\right)\bar{\sigma}^4 - h\bar{\sigma}. \quad (22)$$

$\bar{\sigma} = f_\pi$  gives the minimum of the effective potential at the tree level, and the stationarity condition for the potential (22) gives

$$h = f_\pi m_\pi^2. \quad (23)$$

### A. Polyakov-loop potentials

There are different possibilities for the functional form of the effective Polyakov-loop potential  $\mathcal{U}(\Phi, \bar{\Phi}, T)$ . Its simplest form is constructed by finding a potential that respects all given symmetries and includes the spontaneously broken  $Z(3)$  symmetry for the system in the deconfined phase [2,69,70]. Thus, the minimal content of a Polyakov-loop potential [74] is given by the following polynomial form:

$$\frac{\mathcal{U}_{\text{Poly}}}{T^4} = -\frac{b_2(T)}{2}\Phi\bar{\Phi} - \frac{b_3}{6}(\Phi^3 + \bar{\Phi}^3) + \frac{b_4}{4}(\Phi\bar{\Phi})^2; \quad (24)$$

the coefficients of the Eq. (24) are given by

$$b_2(T) = a_0 + a_1\left(\frac{T_0}{T}\right) + a_2\left(\frac{T_0}{T}\right)^2 + a_3\left(\frac{T_0}{T}\right)^3, \quad (25)$$

where  $a_0 = 6.75$ ,  $a_1 = -1.95$ ,  $a_2 = 2.625$ ,  $a_3 = -7.44$ ,  $b_3 = 0.75$ , and  $b_4 = 7.5$ .

The above Polyakov-loop potential ansatz has been enhanced by adding the contribution that results from the integration of the  $SU(3)$  group volume in the generating functional for the Euclidean action. This integration is done by using the Haar measure and takes the form of a Jacobian determinant. Its logarithm is added as an effective potential to the action in the generating functional. The positive coefficient of the logarithm term bounds the potential from

below for large  $\Phi$  and  $\bar{\Phi}$ , and the logarithmic form of the Polyakov-loop potential is written as [72,75]

$$\begin{aligned} \frac{\mathcal{U}_{\text{Log}}}{T^4} &= b(T) \ln[1 - 6\Phi\bar{\Phi} + 4(\Phi^3 + \bar{\Phi}^3) - 3(\Phi\bar{\Phi})^2] \\ &\quad - \frac{1}{2}a(T)\Phi\bar{\Phi}. \end{aligned} \quad (26)$$

The parameters of the polynomial and Log form of the Polyakov-loop potential were determined [74,75] by fitting the lattice data for pressure, entropy density as well as energy density and the evolution of Polyakov-loop  $\langle\Phi\rangle$  on the lattice in pure gauge theory. The coefficients of the Eq. (26) are the following [75]:

$$a(T) = a_0 + a_1\left(\frac{T_0}{T}\right) + a_2\left(\frac{T_0}{T}\right)^2, \quad (27)$$

$$b(T) = b_3\left(\frac{T_0}{T}\right)^3, \quad (28)$$

where  $a_0 = 3.51$ ,  $a_1 = -2.47$ ,  $a_2 = 15.2$ ,  $b_3 = -1.75$ . Note that the Log potential has qualitative consistency with the leading order result of the strong-coupling expansion [15]. Also, since the potential diverges for  $\Phi, \bar{\Phi} \rightarrow 1$ , the Polyakov-loop always remains smaller than 1 and approaches this value asymptotically as  $T \rightarrow \infty$ .

Reference [82] took into account the Polyakov-loop fluctuations and constructed the new Polyakov-loop effective potential in which the parameters are so adjusted that apart from the other existing lattice data, the lattice data for the longitudinal as well as the transverse susceptibilities are also reproduced. They enhanced the polynomial form of the Polyakov-loop potential with the addition of the logarithmic term to arrive at the following expression of the PolyLog Polyakov-loop potential:

$$\begin{aligned} \frac{\mathcal{U}_{\text{PolyLog}}}{T^4} &= b(T) \ln[1 - 6\Phi\bar{\Phi} + 4(\Phi^3 + \bar{\Phi}^3) - 3(\Phi\bar{\Phi})^2] \\ &\quad + a_2(T)\Phi\bar{\Phi} + a_3(T)(\Phi^3 + \bar{\Phi}^3) + a_4(T)(\Phi\bar{\Phi})^2. \end{aligned} \quad (29)$$

The coefficients of the Eq. (29) PolyLog parametrization are defined as

$$a_i(T) = \frac{a_0^{(i)} + a_1^{(i)}\left(\frac{T_0}{T}\right) + a_2^{(i)}\left(\frac{T_0}{T}\right)^2}{1 + a_3^{(i)}\left(\frac{T_0}{T}\right) + a_4^{(i)}\left(\frac{T_0}{T}\right)^2} \quad (30)$$

$$b(T) = b_0\left(\frac{T_0}{T}\right)^{b_1} [1 - e^{b_2\left(\frac{T_0}{T}\right)^{b_3}}]. \quad (31)$$

The parameters are summarized in the Table I.

The deconfinement phase transition is first order for the pure gauge Yang-Mills theory and  $T_c^{\text{YM}} = T_0 = 270$  MeV.

TABLE I. Parameters of the PolyLog Polyakov-loop potential have been taken from the Ref. [82].

PolyLog	$a_0^{(2)}$	$a_1^{(2)}$	$a_2^{(2)}$	$a_3^{(2)}$	$a_4^{(2)}$
	22.07	-75.7	45.03385	2.77173	3.56403
	$a_0^{(3)}$	$a_1^{(3)}$	$a_2^{(3)}$	$a_3^{(3)}$	$a_4^{(3)}$
	-25.39805	57.019	-44.7298	3.08718	6.72812
	$a_0^{(4)}$	$a_1^{(4)}$	$a_2^{(4)}$	$a_3^{(4)}$	$a_4^{(4)}$
	27.0885	-56.0859	71.2225	2.9715	6.61433
	$b_0$	$b_1$	$b_2$	$b_3$	
	-0.32665	5.8559	-82.9823	3.0	

The first order transition turns to a crossover in the presence of dynamical quarks. The parameter  $T_0$  depends on the number of quark flavors and chemical potential in the full dynamical QCD [55,77,81,84,85] as it is linked to the mass-scale  $\Lambda_{\text{QCD}}$ , which gets modified by the effect of the fermionic matter fields.  $T_0 \rightarrow T_0(N_f, \mu)$  is written as

$$T_0(N_f, \mu) = \hat{T} e^{-1/(\alpha_0 b(N_f, \mu))}, \quad (32)$$

with

$$b(N_f, \mu) = \frac{1}{6\pi} (11N_c - 2N_f) - b_\mu \frac{\mu^2}{(\hat{\gamma} \hat{T})^2}, \quad (33)$$

where the parameter  $\hat{T}$  is fixed at the scale  $\tau$ ,  $\hat{T} = T_\tau = 1.77$  GeV, and  $\alpha_0 = \alpha(\Lambda)$  at a UV scale  $\Lambda$ . The  $T_0(N_f = 0) = 270$  MeV gives  $\alpha_0 = 0.304$  and  $b_\mu \simeq \frac{16}{\pi} N_f$ . The parameter  $\hat{\gamma}$  governs the curvature of  $T_0(\mu)$  with the systematic error estimation range  $0.7 \lesssim \hat{\gamma} \lesssim 1$  [77,85]. In our calculation, we have taken  $\hat{\gamma} = 1$ . The  $N_f, \mu$  dependence of the  $T_0$  accounts only partially for the unquenching of the pure gauge Polyakov-loop potential to an effective glue potential in QCD [84].

For the full QCD with dynamical quarks, the Polyakov-loop potential should be replaced by the QCD glue potential that accounts for the backreaction of quarks into the Polyakov-loop effective potential. Applying the FRG equations to the QCD, Ref. [81] compared the pure gauge potential  $\mathcal{U}_{\text{YM}}$  to the “glue” potential  $\mathcal{U}_{\text{glue}}$ , where quark polarization was included in the gluon propagator, and they found significant differences between the two potentials. However, it was observed in their study that the two potentials have the same shape, and they can be mapped into each other by relating the temperatures of the two systems,  $T_{\text{YM}}$  and  $T_{\text{glue}}$ . Denoting the previous equations of the Polyakov-loop potential by  $\mathcal{U}_{\text{YM}}$ , the improved Polyakov-loop potential  $\mathcal{U}_{\text{glue}}$  can be constructed as [81]

$$\frac{\mathcal{U}_{\text{glue}}}{T_{\text{glue}}^4}(\Phi, \bar{\Phi}, T_{\text{glue}}) = \frac{\mathcal{U}_{\text{YM}}}{T_{\text{YM}}^4}(\Phi, \bar{\Phi}, T_{\text{YM}}). \quad (34)$$

Here, the temperature  $T_{\text{glue}}$  is related to  $T_{\text{YM}}$  as

$$\frac{T_{\text{YM}} - T_c^{\text{YM}}}{T_c^{\text{YM}}} = 0.57 \frac{T_{\text{glue}} - T_c^{\text{glue}}}{T_c^{\text{glue}}}. \quad (35)$$

The  $T_c^{\text{glue}}$  is the transition temperature for the unquenched case. The coefficient 0.57 comes from the comparison of the two effective potentials.  $T_c^{\text{glue}}$  lies within a range  $T_c^{\text{glue}} \in [180, 270]$ . In practice, we use in the right-hand side of the Polyakov-loop potentials, where  $T_0$  means  $T_c^{\text{YM}}$ , the replacement  $T \rightarrow T_c^{\text{YM}}(1 + 0.57(\frac{T}{T_c^{\text{glue}}} - 1))$ , where ( $T \sim T_{\text{YM}}$ ) on the left side of the arrow and ( $T \sim T_{\text{glue}}$ ) on the right side. In our calculations, we will keep  $T_c^{\text{glue}}$  and  $T_0$  both fixed at 208 MeV and also consider the chemical potential dependence of  $T_0$  and  $T_c^{\text{glue}}$ . The  $\mu$  dependence of the  $T_c^{\text{glue}}$  can be found from the Eq. (32) after making the replacement  $T_0(N_f, \mu) \rightarrow T_c^{\text{glue}}(N_f, \mu)$ .

## B. Thermodynamic grand potential in PQM model

In the mean-field approximation, the thermodynamic grand potential for the PQM model is given as [77]

$$\Omega_{\text{MF}}(T, \mu; \bar{\sigma}, \Phi, \bar{\Phi}) = U(\bar{\sigma}) + \Omega_{q\bar{q}}(T, \mu; \bar{\sigma}, \Phi, \bar{\Phi}) + \mathcal{U}(T, \Phi, \bar{\Phi}). \quad (36)$$

The quark/antiquark contribution is given by

$$\Omega_{q\bar{q}}(T, \mu; \bar{\sigma}, \Phi, \bar{\Phi}) = \Omega_{q\bar{q}}^{\text{vac}} + \Omega_{q\bar{q}}^{T, \mu}, \quad (37)$$

$$\Omega_{q\bar{q}}^{\text{vac}} = -2N_c \sum_q \int \frac{d^3 p}{(2\pi)^3} E_q \theta(\Lambda_c^2 - \vec{p}^2), \quad (38)$$

$$\Omega_{q\bar{q}}^{T, \mu}(\bar{\sigma}, \Phi, \bar{\Phi}) = -2N_c \sum_q \int \frac{d^3 p}{(2\pi)^3} T [\ln g_q^+ + \ln g_q^-]. \quad (39)$$

The first term of the Eq. (37) denotes the fermion vacuum contribution, regularized by the ultraviolet cutoff  $\Lambda_c$ . In presence of the Polyakov-loop potential, the  $g_q^+$  and  $g_q^-$  are specified by the trace in the color space,

$$g_q^+ = \left[ 1 + 3\Phi e^{-E_q^+/T} + 3\bar{\Phi} e^{-2E_q^+/T} + e^{-3E_q^+/T} \right], \quad (40)$$

$$g_q^- = \left[ 1 + 3\bar{\Phi} e^{-E_q^-/T} + 3\Phi e^{-2E_q^-/T} + e^{-3E_q^-/T} \right]. \quad (41)$$

$E_q^\pm = E_q \mp \mu_q$  and  $E_q = \sqrt{p^2 + m_q^2}$  is the flavor dependent single particle energy of quark/antiquark, and  $m_q = \frac{q\bar{\sigma}}{2}$  is the mass of the given quark flavor.  $\mu_q$  is the quark chemical potential.

Neglecting the quark one-loop vacuum term of the Eq. (37) in the standard mean-field approximation (s-MFA), the PQM model grand potential is written as

$$\Omega_{\text{PQM}}(T, \mu; \bar{\sigma}, \Phi, \bar{\Phi}) = U(\bar{\sigma}) + \Omega_{q\bar{q}}^{T, \mu}(\bar{\sigma}, \Phi, \bar{\Phi}) + \mathcal{U}(T, \Phi, \bar{\Phi}), \quad (42)$$

$$\frac{\partial \Omega_{\text{PQM}}}{\partial \bar{\sigma}} = \frac{\partial \Omega_{\text{PQM}}}{\partial \Phi} = \frac{\partial \Omega_{\text{PQM}}}{\partial \bar{\Phi}} \Big|_{\bar{\sigma}, \Phi, \bar{\Phi}} = 0. \quad (43)$$

The global minima of the grand potential in Eq. (43) gives the  $\bar{\sigma}$ ,  $\Phi$ , and  $\bar{\Phi}$  as a function of temperature and chemical potential.

### III. PQM MODEL WITH VACUUM TERM

Here, we give a brief description of the effective potential calculation when the quark one-loop vacuum divergence of the Eq. (37) is regularized in the minimal subtraction scheme, and the  $\sigma$  and  $\pi$  meson curvature masses are used for fixing the model parameters. The quark one-loop vacuum contribution of Eq. (38) is written as [67]

$$\Omega_{q\bar{q}}^{\text{vac}} = \frac{N_c}{(4\pi)^2} \sum_q m_q^4 \left[ \frac{1}{\epsilon} + \frac{3}{2} + \ln \left( \frac{\Lambda^2}{m_q^2} \right) \right], \quad (44)$$

where  $\Lambda$  is the renormalization scale.

Adding the counterterm  $\delta \mathcal{L} = \frac{N_c}{(4\pi)^2} \sum_q \frac{m_q^4}{\epsilon}$  to the Lagrangian (4), the thermodynamic potential gets renormalized. After replacing the first term of Eq. (37) by the  $\Omega_{q\bar{q}}^{\text{vac}} = \frac{N_c}{(4\pi)^2} \sum_q m_q^4 \left[ \frac{3}{2} + \ln \left( \frac{\Lambda^2}{m_q^2} \right) \right]$ , one gets the renormalization scale dependent chiral part of the vacuum ( $\mu = 0$  and  $T = 0$ ) effective potential as

$$\Omega^\Lambda(\bar{\sigma}) = U(\bar{\sigma}) + \Omega_{q\bar{q}}^{\text{vac}}. \quad (45)$$

The fixing of the model parameters  $m^2$ ,  $c$ ,  $\lambda_1$ ,  $\lambda_2$ , and  $h$  is presented in Appendix A. When the calculated new parameters are substituted in the Eq. (45) and terms are rearranged, one finds the expression of renormalization scale  $\Lambda$  independent vacuum effective potential as

$$\begin{aligned} \Omega(\bar{\sigma}) = & \frac{1}{2} \left( m_s^2 - \frac{N_c g^4 f_\pi^2}{2(4\pi)^2} \right) \bar{\sigma}^2 - \frac{1}{2} c \bar{\sigma}^2 + \frac{1}{4} \left( \lambda_1 + \frac{\lambda_{2s}}{2} \right. \\ & \left. + \frac{3N_c g^4}{4(4\pi)^2} \right) \bar{\sigma}^4 - h \bar{\sigma} + \frac{N_c g^4 \bar{\sigma}^4}{8(4\pi)^2} \ln \left( \frac{f_\pi^2}{\bar{\sigma}^2} \right). \end{aligned} \quad (46)$$

After quark one-loop vacuum correction, the thermodynamic grand potential for the Polyakov-loop enhanced quark-meson model with vacuum term (PQMVT) can be written as

$$\Omega_{\text{PQMVT}}(T, \mu; \bar{\sigma}, \Phi, \bar{\Phi}) = \Omega(\bar{\sigma}) + \Omega_{q\bar{q}}^{T, \mu}(\bar{\sigma}, \Phi, \bar{\Phi}) + \mathcal{U}(\Phi, \bar{\Phi}), \quad (47)$$

$$\frac{\partial \Omega_{\text{PQMVT}}}{\partial \bar{\sigma}} = \frac{\partial \Omega_{\text{PQMVT}}}{\partial \Phi} = \frac{\partial \Omega_{\text{PQMVT}}}{\partial \bar{\Phi}} \Big|_{\bar{\sigma}, \Phi, \bar{\Phi}} = 0. \quad (48)$$

One gets the quark condensate  $\bar{\sigma}$  and the Polyakov-loop expectation values  $\Phi$ ,  $\bar{\Phi}$  by searching the global minima of the grand potential at a given  $T$  and  $\mu$ . It is pointed out that the pion decay constant  $f_\pi$  does not get renormalized because the dressing of the meson propagator is not considered in fixing of the model parameters using the curvature mass of the pion. The minimum of the effective potential in vacuum ( $T = 0$ ,  $\mu = 0$ ) remains fixed at  $\bar{\sigma} = f_\pi$ .

### IV. RENORMALIZED PQM MODEL

The PQMVT/QMVT model investigations [45–58] use the curvature (or screening) masses of the mesons to fix the parameters while the pion decay constant  $f_\pi$  remains unrenormalized. We know that the poles of the mesons propagators give their physical masses, and the  $f_\pi$  gets a correction as it is related to the residue of the pion propagator at its pole [61–63]. The definition of the meson curvature masses involves the evaluation of their self-energies at zero momentum as the effective potential is the generator of the n-point functions of the theory at zero external momenta [59,60,64,65]. Furthermore, the pole definition is the physical and gauge invariant one [86,87]. If the Dirac sea contributions are neglected, the pole masses and the curvature masses for mesons become equivalent, but when the quark one-loop vacuum correction is considered, the curvature masses of the mesons become different from their pole masses [61,63]. The above inconsistency is removed in the exact on-shell parameter fixing method of the renormalized quark-meson (RQM) model, where the physical (pole) masses of the mesons and the pion decay constant are put into the relation of the running mass parameter and couplings by using the on-shell and the minimal subtraction renormalization schemes. The derivation of the quark one-loop effective potential in the large  $N_c$  limit and the mathematical details of the on-shell parameter fixing for the renormalized quark-meson (RQM) model have been presented in Appendix B. Combining the RQM model chiral effective potential in  $\overline{\text{MS}}$  scheme with the Polyakov-loop potential, we get grand thermodynamic potential for the RPQM model as

$$\begin{aligned} \Omega_{\text{RPQM}}(T, \mu; \Delta, \Phi, \bar{\Phi}) = & \Omega_{\text{vac}}(\Delta) + \Omega_{q\bar{q}}^{T, \mu}(\Delta, \Phi, \bar{\Phi}) \\ & + \mathcal{U}(\Phi, \bar{\Phi}). \end{aligned} \quad (49)$$

Using the expression  $\Omega_{\text{vac}}(\Delta)$  of Eq. (B77) given in Appendix B, we write the full thermodynamic potential for the RPQM model as

TABLE II. Parameters of the different model scenarios. The RPQM model parameters are obtained by putting the  $\Lambda = \Lambda_0$  in the Eqs. (B53)–(B57). The  $\Lambda_0$  is determined from the condition (B74). The parameters of the PQM model are used to compute the effective potential of the PQMVT model in the Eq. (46).

Model	$m_\sigma$ (MeV)	$c$ (MeV <sup>2</sup> )	$m^2$ (MeV <sup>2</sup> )	$\lambda_1$	$\lambda_2$	$h$ (MeV <sup>3</sup> )
PQM	400	(374.28) <sup>2</sup>	(297.74) <sup>2</sup>	−30.61	77.51	(120.99) <sup>3</sup>
	500	(374.28) <sup>2</sup>	(208.92) <sup>2</sup>	−25.41	77.51	(120.99) <sup>3</sup>
	600	(374.28) <sup>2</sup>	−(106.54) <sup>2</sup>	−19.05	77.51	(120.99) <sup>3</sup>
RPQM	400	(494.08) <sup>2</sup>	(282.13) <sup>2</sup>	−28.05	66.94	(119.8) <sup>3</sup>
	500	(494.08) <sup>2</sup>	(196.80) <sup>2</sup>	−23.32	66.94	(119.8) <sup>3</sup>
	600	(494.08) <sup>2</sup>	−(202.13) <sup>2</sup>	−14.12	66.94	(119.8) <sup>3</sup>
	616	(494.08) <sup>2</sup>	−(253.86) <sup>2</sup>	−11.39	66.94	(119.8) <sup>3</sup>
	700	(494.08) <sup>2</sup>	−(421.55) <sup>2</sup>	1.70	66.94	(119.8) <sup>3</sup>

$$\begin{aligned}
\Omega_{\text{RPQM}}(T, \mu; \Delta, \Phi, \bar{\Phi}) = & \frac{(3m_\pi^2 - m_\sigma^2)f_\pi^2}{4} \left\{ 1 - \frac{N_c g^2}{(4\pi)^2} (C(m_\pi^2) + m_\pi^2 C'(m_\pi^2)) \right\} \frac{\Delta^2}{m_q^2} \\
& + \frac{N_c g^2 f_\pi^2}{2(4\pi)^2} \left\{ \frac{3m_\pi^2 C(m_\pi^2) - (m_\sigma^2 - 4m_q^2)C(m_\sigma^2)}{2} - 2m_q^2 \right\} \frac{\Delta^2}{m_q^2} \\
& + \frac{(m_\sigma^2 - m_\pi^2)f_\pi^2}{8} \left\{ 1 - \frac{N_c g^2}{(4\pi)^2} (C(m_\pi^2) + m_\pi^2 C'(m_\pi^2)) \right\} \frac{\Delta^4}{m_q^4} \\
& + \frac{N_c g^2 f_\pi^2}{(4\pi)^2} \left[ \frac{(m_\sigma^2 - 4m_q^2)C(m_\sigma^2) - m_\pi^2 C(m_\pi^2)}{8} \frac{\Delta^4}{m_q^4} + \frac{2N_c \Delta^4}{(4\pi)^2} \left\{ \frac{3}{2} - \ln \left( \frac{\Delta^2}{m_q^2} \right) \right\} \right] \\
& - m_\pi^2 f_\pi^2 \left\{ 1 - \frac{N_c g^2}{(4\pi)^2} m_\pi^2 C'(m_\pi^2) \right\} \frac{\Delta}{m_q} + \Omega_{q\bar{q}}^{T,\mu}(\Delta, \Phi, \bar{\Phi}) + \mathcal{U}(\Phi, \bar{\Phi}); \tag{50}
\end{aligned}$$

$$\frac{\partial \Omega_{\text{RPQM}}}{\partial \Delta} = \frac{\partial \Omega_{\text{RPQM}}}{\partial \Phi} = \frac{\partial \Omega_{\text{RPQM}}}{\partial \bar{\Phi}} \Big|_{\Delta, \Phi, \bar{\Phi}} = 0. \tag{51}$$

Searching the global minima of the grand potential for a given  $\mu$  and  $T$ , one gets the quark condensate  $\bar{\sigma}$  ( $\Delta = \frac{g_{\text{MS}} \bar{\sigma}_{\text{MS}}}{2}$ ), and the Polyakov-loop fields  $\Phi$  and  $\bar{\Phi}$ . It has been explained in Appendix B that the minimum of the vacuum ( $T = 0, \mu = 0$ ) effective potential remains at  $\bar{\sigma}_{\text{MS}} = f_\pi$ . In our calculations, we have used the  $m_\pi = 138.0$  MeV,  $m_{a_0} = 984.7$  MeV, and  $m_\eta = 547.0$  MeV. The Yukawa coupling  $g = 6.5$  and pion decay constant  $f_\pi = 93.0$  MeV. The constituent quark mass in the vacuum  $m_q = \frac{gf_\pi}{2} = 302.25$  MeV. The parameters of different models have been presented in the Table II.

## V. RESULTS AND DISCUSSION

The temperature axis chiral crossover and confinement-deconfinement crossover transition at  $\mu = 0$  has been thoroughly investigated and compared with, in different model scenarios of combining, the chiral effective potential computed in different parameter fixing schemes to the

different forms of the Polyakov-loop potential with and without quark backreaction. The subsection A compares the results for the temperature variations of the chiral condensate, the Polyakov-loop condensate and their derivatives. The chiral and deconfinement crossover transition temperatures for different model scenarios have been computed and presented for comparison in Tables III and IV. In the subsection B, the PQM, PQMVT, and RPQM model phase diagrams have been plotted and compared with each other for different values of  $m_\sigma$  and different forms of the Polyakov-loop potentials with

TABLE III. Pseudocritical temperatures for the  $m_\sigma = 500$  MeV at  $\mu = 0$ .

Polyakov-loop	Models	$T_c^\chi$ (MeV)	$T_c^\Phi$ (MeV)
Log	PQM	172.1	168.9
	PQMVT	187.1	168.9
	RPQM	168.6	167.9
PolyLog-gluon	PQM	165.6	165.4
	PQMVT	186.3	156.1
	RPQM	175.8	154.8

TABLE IV. Pseudocritical temperatures for the  $m_\sigma = 500$  MeV in the RPQM model at  $\mu = 0$ .

Models	$T_c^\chi$ (MeV)	$T_c^\Phi$ (MeV)
Log	168.6	167.9
Log-glu	174.6	145.2
Poly	181.6	176.6
Poly-glu	174.8	159.8
PolyLog	180.1	175.1
PolyLog-glu	175.8	154.8

and without quark backreaction. The appearance and disappearance of the quarkyonic phase in different model scenarios have been discussed in the subsection C. In order to understand the  $\mu = 0$  chiral and deconfinement transition occurring at the temperature axis, we have computed and compared the reduced scale temperature variations of the thermodynamic quantities namely the pressure, entropy density, energy density, and interaction measure in the subsection D while the results for the specific heat,  $C_s^2$  and  $P/\epsilon$  have been presented in the subsection E. We have also compared the results obtained for thermodynamic observables with the available lattice QCD data.

### A. Order parameters and their derivatives

Figures 1(a) and 1(b) present the respective temperature variations of the normalized chiral condensate ( $\sigma/f_\pi$ ) and the Polyakov-loop condensate ( $\Phi$ ) at  $\mu = 0$  for the sigma mass  $m_\sigma = 500$  MeV in the PQM, PQMVT, and RPQM model for the Log and the PolyLog-glu form of the Polyakov-loop potential. The term glu denotes the unquenching of the Polyakov-loop potential when the quark back-reaction has been taken into account.

Confirming the expected pattern when the models are augmented with the Log form of the Polyakov-loop potential, the sharper Log-PQM model chiral transition becomes quite smooth and delayed on account of the quark one-loop vacuum correction in the on-shell renormalized Log-RPQM model while the curvature mass parametrization for the Log-PQMVT model gives rise to an excessively smooth and very delayed variation of the chiral order parameter on the temperature axis in the Fig. 1(a). When the physics of the confinement-deconfinement transition is coupled with the physics of the chiral transition, the unquenching of the Polyakov-loop potential in the presence of the quark backreaction, leads to the significant smoothing effect on the chiral condensate and shifts its temperature variations early on the temperature scale for the  $T < 190$  MeV in the PolyLog-glu: PQM, RPQM, and PQMVT model. Furthermore, the Polyakov-loop condensate temperature variations are lifted up and get shifted early on the temperature scale for the  $T < 220$  MeV, due to the effect of the quark backreaction when compared to the corresponding PQM, RPQM and PQMVT model temperature variations with Log form of the Polyakov-loop potential in the Fig. 1(b).

Presenting the plots of the  $\frac{\partial(\sigma/f_\pi)}{\partial T}$  and  $\frac{\partial\Phi}{\partial T}$  versus  $T$  when the  $\mu = 0$  and the  $m_\sigma = 500$  MeV in the Figs. 2(a)–2(c), respectively, for the PQM, PQMVT, and RPQM model with the Log and PolyLog-glu form of the Polyakov-loop potential, we have compared how the PQM model results are changed by the effect of the quark one-loop vacuum correction in the curvature mass parametrized PQMVT model versus the on-shell parametrized RPQM model. We have also compared how the presence of the quark backreaction changes the results in one particular model. For the Log-PQM model in the Fig. 2(a), the very sharp

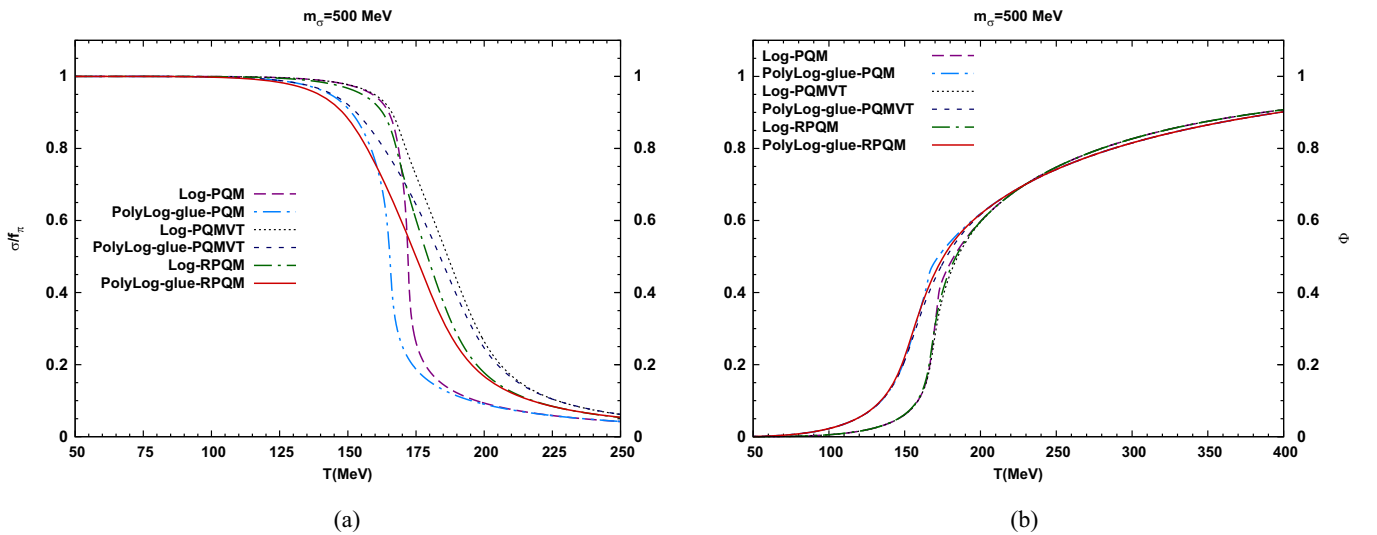


FIG. 1. The normalized chiral and Polyakov-loop order parameters for the  $m_\sigma = 500$  MeV and  $\mu = 0$  at  $T_c^{\text{gluc}} = T_0 = 208$  MeV. (a) Normalized chiral condensate. (b) Polyakov-loop order parameter.

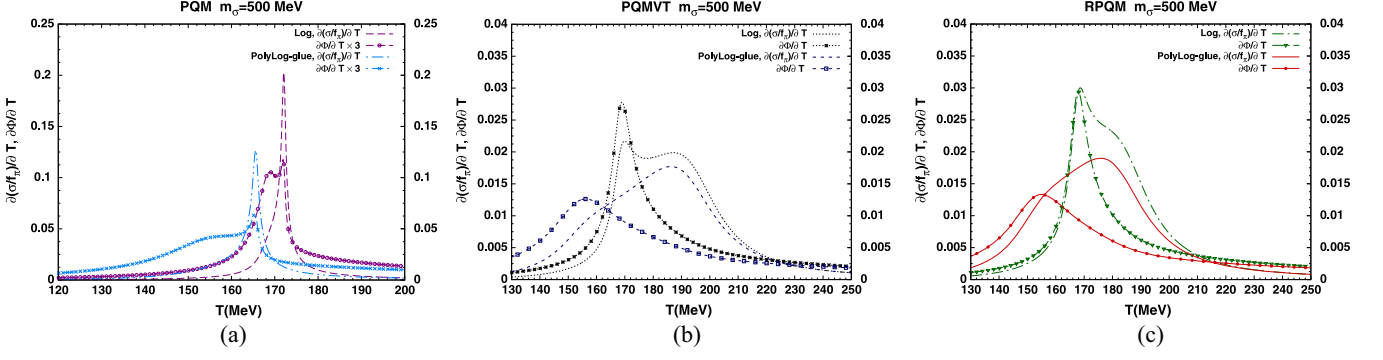


FIG. 2. The derivatives of the normalized chiral and Polyakov-loop order parameters for the  $\mu = 0$  and  $T_c^{\text{gluc}} = T_0 = 208$  MeV. The temperature variation of the  $\frac{\partial(\sigma/f_\pi)}{\partial T}$  and  $\frac{\partial\Phi}{\partial T}$  with the Log and PolyLog-gluon form of the Polyakov-loop potential in the (a) PQM model (b) PQMVT model (c) RPQM model.

variation of the temperature derivative of the  $\sigma/f_\pi$  drives a double peak structure in the temperature variation of the  $\frac{\partial\Phi}{\partial T}$ , whose first peak at lower temperature gives a pseudo-critical temperature  $T_c^\Phi = 168.9$  MeV for the confinement-deconfinement transition and its second peak coincides with the very sharp and high peak in the  $\frac{\partial(\sigma/f_\pi)}{\partial T}$  variation, which gets located at the higher pseudocritical temperature for the chiral transition  $T_c^\chi = 172.1$  MeV and the two transitions are separated by the difference  $T_c^\chi - T_c^\Phi = 3.2$  MeV as given in the Table III. One notices that the double peak structure for the  $\frac{\partial\Phi}{\partial T}$  is smoothed out and the sharper chiral transition also becomes quite smooth as the peak heights get significantly reduced due to the effect of the quark backreaction in the PolyLog-gluon PQM model, and the two transitions stand very close to each other having a difference of only 0.2 MeV as the  $T_c^\chi = 165.6$  MeV and the  $T_c^\Phi = 165.4$  MeV. As the fermionic vacuum correction with the curvature mass parametrization leads to excess smoothing of the chiral transition, the  $\frac{\partial(\sigma/f_\pi)}{\partial T}$  variation for the Log PQMVT model shows a very smooth double peak structure (similar to Ref. [46]) in the Fig. 2(b). Here, in contrast to the Fig. 2(a), the influence of the Log form of the Polyakov-loop potential becomes dominant and the sharper temperature variation of the  $\frac{\partial\Phi}{\partial T}$  generates a double peak for the  $\frac{\partial(\sigma/f_\pi)}{\partial T}$  variation and the separation between the chiral crossover and the confinement-deconfinement transition is equal to the 18.2 MeV as the  $T_c^\chi = 187.1$  MeV and the  $T_c^\Phi = 168.9$  MeV in Table III. It is to be noted that due to the smoothing influence of the quark backreaction for the unquenched PolyLog-gluon PQMVT model, the double peak of the  $\frac{\partial(\sigma/f_\pi)}{\partial T}$  variation gets completely washed out, and one gets largest separation of 30.2 MeV between the confinement-deconfinement and the chiral crossover transition temperatures as the  $T_c^\chi = 186.3$  MeV while the  $T_c^\Phi = 156.1$  MeV. The smoothing influence of the quark one-loop vacuum correction becomes moderate due to the consistent on-shell parameter fixing for the RPQM model and one

notices that the temperature variations of the  $\frac{\partial\Phi}{\partial T}$  and the  $\frac{\partial(\sigma/f_\pi)}{\partial T}$  rise to almost the same height in the Fig. 2(c) for the Log form of the Polyakov-loop potential in the RPQM model. The  $\frac{\partial(\sigma/f_\pi)}{\partial T}$  variation falls short of developing a second peak, and one finds that the chiral crossover transition at the  $T_c^\chi = 168.6$  MeV is very close to the confinement-deconfinement transition occurring at the  $T_c^\Phi = 167.9$  MeV. Here, also in the unquenched PolyLog-gluon RPQM model, the robust effect of the quark backreaction leads to sufficient smoothing and reduction in the heights of the peaks of the  $\frac{\partial\Phi}{\partial T}$  and  $\frac{\partial(\sigma/f_\pi)}{\partial T}$  temperature variations, and a moderate separation of 21.0 MeV is noted between the confinement-deconfinement and the chiral crossover transition temperatures as the  $T_c^\chi = 175.8$  MeV while the  $T_c^\Phi = 154.8$  MeV.

The Figs. 3(a) and 3(b) show how the respective temperature variations of the  $\sigma/f_\pi$  and  $\Phi$  are influenced by the different forms of the Polyakov-loop potential put in combination with the consistent formulation of the chiral sector physics in the RPQM model. The falling patterns of the  $\sigma/f_\pi$  in the Fig. 3(a), shift early on the temperature scale because of the quark back-reaction in the unquenched forms of the Polyakov-loop potentials namely the Log-gluon, Poly-gluon, and PolyLog-gluon. The lattice QCD data for the temperature variation of the  $\Phi$  has also been plotted in the Fig. 3(b). One can see that the RPQM model Polyakov-loop condensate temperature variations for the Log and the PolyLog potential are closer to the [88,89] lattice results when the  $T < 170$  MeV. For higher temperatures, the  $\Phi$  variation of the Log, the Log-gluon, and the PolyLog-gluon RPQM model, stand closer to the two flavor LQCD data of the Ref. [88].

The Polyakov-loop potential in the Log form has a stronger influence as one notes that the quite sharp peaks of the temperature variations of the  $\frac{\partial(\sigma/f_\pi)}{\partial T}$  and the  $\frac{\partial\Phi}{\partial T}$  are of almost the same height in the Log-RPQM model in the Fig. 4(a), while the corresponding peaks are round and smoother, respectively, for the polynomial and polynomial

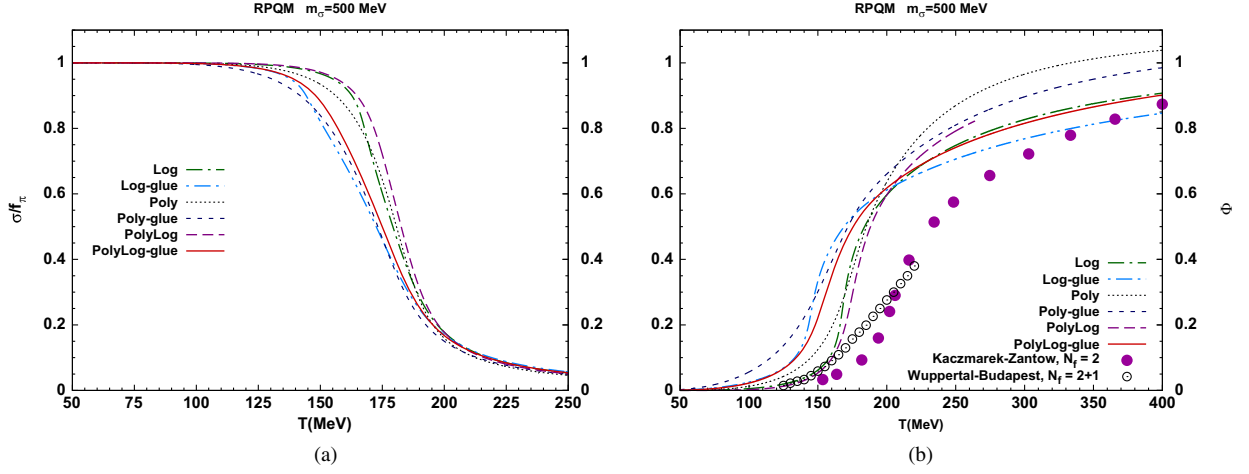


FIG. 3. The RPQM model normalized chiral and Polyakov-loop order parameters when  $\mu = 0$  and  $T_c^{\text{gluc}} = T_0 = 208$  MeV. (a) Normalized chiral condensate. (b) Polyakov-loop order parameter.

combined with the Log form of the Polyakov-loop potential in the Figs. 4(b) and 4(c). Since the height of the  $\frac{\partial(\sigma/f_\pi)}{\partial T}$  peaks are larger than that of the  $\frac{\partial\Phi}{\partial T}$  peaks in the Figs. 4(b) and 4(c), the chiral order parameter temperature variation has stronger influence in the Poly-RPQM and PolyLog-RPQM models. Even though the height of the  $\frac{\partial\Phi}{\partial T}$  peak is reduced and its sharpness gets moderated due to the quark backreaction in the Log-gluon RPQM model in the Fig. 4(a), the Log contribution makes the influence of the Polyakov-loop potential stronger which gives rise to a double peak structure in the temperature variation of the  $\frac{\partial(\sigma/f_\pi)}{\partial T}$ . The quark backreaction has significant smoothing effect on both the order parameters as the  $\frac{\partial(\sigma/f_\pi)}{\partial T}$  and the  $\frac{\partial\Phi}{\partial T}$  temperature variations become more flat and rounded with reduced heights in the Figs. 4(b) and 4(c), respectively, for the Poly-gluon and the PolyLog-gluon RPQM model. It is worth reminding ourselves that the separation ( $T_c^\chi - T_c^\Phi$ ) between the pseudocritical temperatures for the chiral

transition and the confinement-deconfinement transition is very small of only 0.7 MeV for the Log Polyakov-loop potential, and it increases to 5.0 MeV when one has either the Poly or the PolyLog form of the Polyakov-loop potential. One can see from the Table IV that the quark backreaction causes the largest separation of 29.4 MeV in the Log-gluon form while the separation becomes 15 MeV for the Poly-gluon form and 21 MeV for the PolyLog-gluon form of the unquenched Polyakov-loop potential in the RPQM model.

## B. Sigma mass and model dependence of the phase diagrams and CEPs

We have plotted and compared the phase boundaries in the chemical potential and temperature  $\mu - T$  plane for the chiral symmetry breaking-restoring phase transitions in the Polyakov-loop enhanced chiral models, namely the PQM, PQMVT, and RPQM having different forms of parametrization for the Polyakov-loop potential. It is well-known that the first order transition line shrinks and the crossover

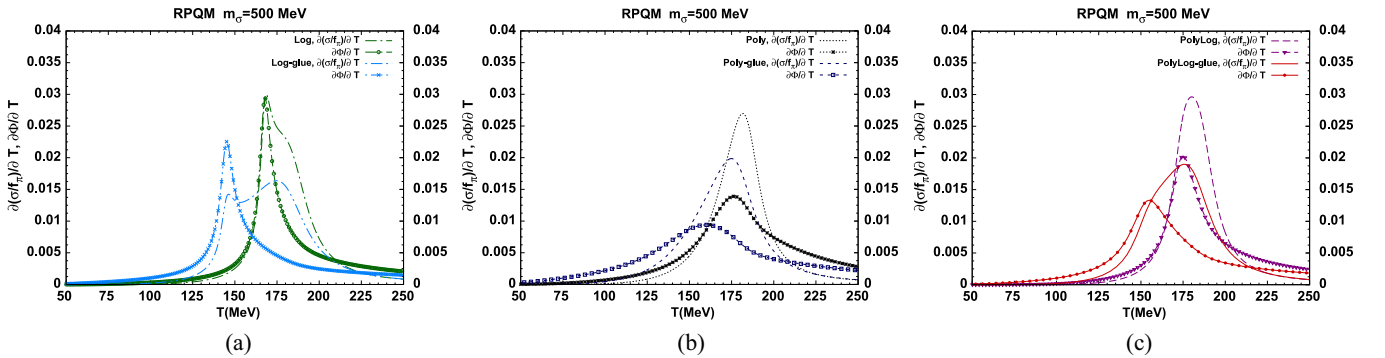


FIG. 4. The derivatives of the normalized chiral and Polyakov-loop order parameters at  $\mu = 0$  and  $T_c^{\text{gluc}} = T_0 = 208$  MeV. The temperature variation of the  $\frac{\partial(\sigma/f_\pi)}{\partial T}$  and  $\frac{\partial\Phi}{\partial T}$  for the RPQM model with the Polyakov-loop potential in the (a) Log and Log-gluon form (b) Poly and Poly-gluon form (c) PolyLog and PolyLog-gluon form.

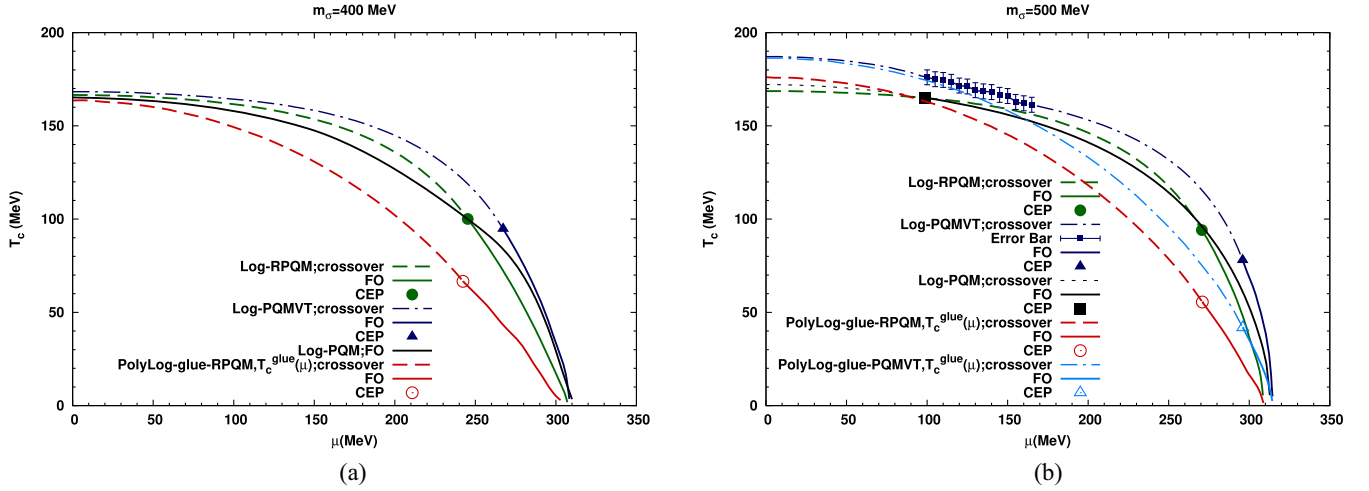


FIG. 5. The PQM, PQMVT, and RPQM model phase diagrams for different forms of the Polyakov-loop potentials. The error bars of the  $\pm 4$  MeV on the Log PQMVT model crossover transition line have been calculated as in Ref. [46].

line gets extended with the increase of sigma meson mass, and therefore, the CEP shifts rightwards in the phase diagram. Below we are presenting phase diagrams for different sigma meson masses. Line types in all the phase diagrams are labeled and explained in the figures.

The Fig. 5(a) presents the phase diagram for the  $m_\sigma = 400$  MeV. The complete phase boundary for the Log PQM model is a first order phase transition line. Since the quark one-loop vacuum correction with the curvature mass parametrization in the Log PQMVT generates excessively smooth chiral transition as also reported in earlier works [46,47,50], one gets a longer length of the line depicting the chiral crossover transition that terminates at the critical end point (CEP) at  $\mu_{\text{CEP}} = 267.2$  MeV,  $T_{\text{CEP}} = 94.77$  MeV, and the phase boundary becomes the first order transition line afterwards. The on-shell parameter fixing for the Log-RPQM model with the consistent renormalization of the quark one-loop vacuum correction gives rise to a relatively moderate smoothing effect on the chiral transition, and the CEP gets located higher up in the  $\mu - T$  plane at the  $T_{\text{CEP}} = 100.1$  MeV and the  $\mu_{\text{CEP}} = 245.3$  MeV. When we consider the chemical potential dependence of the parameter  $T_0 \equiv T_0(\mu) = T_c^{\text{glue}}(\mu)$  together with the unquenched PolyLog-gluon form of the Polyakov-loop potential in the RPQM model, the quark backreaction generates an additional robust smoothing influence on the chiral transition due to which the CEP shifts downwards and gets located at  $\mu_{\text{CEP}} = 242.3$  MeV and  $T_{\text{CEP}} = 66.6$  MeV. Note that the influence of the quark backreaction is quite strong in the temperature direction as the PolyLog-gluon RPQM model  $T_{\text{CEP}}$  shifts down by 33.5 MeV when compared with the  $T_{\text{CEP}}$  of the Log RPQM model, while the corresponding shift in the chemical potential  $\mu_{\text{CEP}}$  is only 3 MeV. This effect gives rise to the increased curvature of the phase transition line as first reported and discussed in the Ref. [84]. We point out that in

our recent work [67] in the on-shell renormalized quark-meson (RQM) model where the effect of the Polyakov-loop potential is absent, the CEP gets located in the bottom right of the  $\mu - T$  plane at  $T_{\text{CEP}} = 38.2$  MeV and  $\mu_{\text{CEP}} = 253.5$  MeV when the  $m_\sigma = 400$  MeV. We see that the presence of Polyakov-loop potential either in the Log or in the PolyLog-gluon form in the RPQM model leads to significant upward shift of the CEP in the  $\mu - T$  plane.

The phase diagram for the  $m_\sigma = 500$  MeV case has been plotted in the Fig. 5(b). We get a small crossover line ending in the critical end point at  $T_{\text{CEP}} = 165.1$  MeV and  $\mu_{\text{CEP}} = 98.8$  MeV and a quite long first order line for the Log-PQM model. In the Log-PQMVT model, similar to the  $m_\sigma = 400$  MeV case, the crossover line becomes very large at the expense of significantly shrunk first order region, and the CEP gets located at  $T_{\text{CEP}} = 78.0$  MeV,  $\mu_{\text{CEP}} = 295.9$  MeV. When we consider the unquenched PolyLog-gluon form for the Polyakov-loop potential with the chemical potential dependent parameter  $T_0 \equiv T_0(\mu) = T_c^{\text{glue}}(\mu)$ , the quark backreaction in the PolyLog-gluon PQMVT model causes 36.2 MeV reduction in the temperature axis location of the CEP when compared with the  $T_{\text{CEP}}$  of the Log-PQMVT model as it gets located at the  $T_{\text{CEP}} = 41.8$  MeV, while the chemical potential location remains almost the same at the  $\mu_{\text{CEP}} = 296.0$  MeV. Note that the uncertainty bar of the Log PQMVT model for finding the  $T_c^{\text{glue}}$  in the chemical potential range 100–165 MeV, also disappears in the PolyLog-gluon PQMVT model, and we find a well-defined crossover transition line with increased curvature. When compared to the CEP of the Log PQMVT model, the CEP in the Log RPQM model gets located higher up on the temperature axis at  $T_{\text{CEP}} = 94.1$  MeV with smaller chemical potential at  $\mu_{\text{CEP}} = 270.6$  MeV. The above result is expected because the smoothing influence of the on-shell renormalized quark one-loop vacuum fluctuation on the

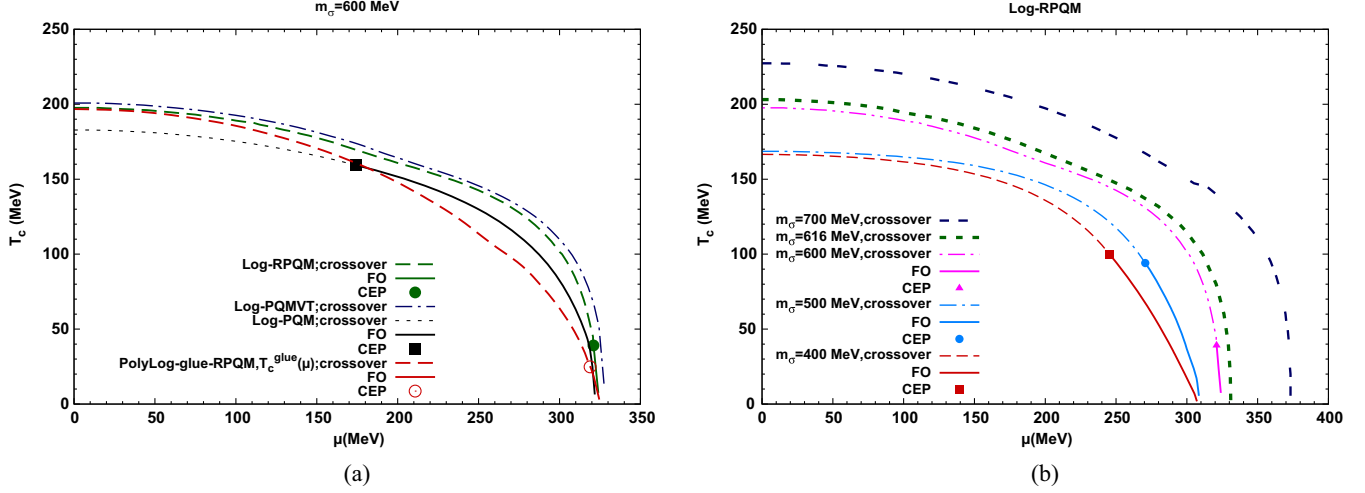


FIG. 6. Phase diagrams in the (a) are for the PQM, PQMVT, and RPQM model and in the (b) are for the different  $m_\sigma$  in the Log RPQM model.

chiral transition remains moderate also when the  $m_\sigma = 500$  MeV [67]. The CEP of the Log RPQM model shifts down in temperature by 38.5 MeV due to the effect of quark backreaction in the unquenched PolyLog-gluon RPQM model with  $T_0 \equiv T_0(\mu) = T_c^{\text{glue}}(\mu)$  and gets located at the  $T_{\text{CEP}} = 55.6$  MeV, while the corresponding chemical potential gets located at the  $\mu_{\text{CEP}} = 270.9$  MeV with a negligible shift. When the  $\mu$  dependence of the  $T_0$  is switched off in the PolyLog-gluon RPQM model as shown later in the Fig. 7(a), the CEP gets located at the  $T_{\text{CEP}} = 70.1$  MeV and the  $\mu_{\text{CEP}} = 268.1$  MeV with a moderate temperature axis shift of 24.0 MeV in reference to the CEP of the Log RPQM model. The curvature of the phase transition line increases significantly for all the cases where the unquenching of the Polyakov-loop potential has been considered. In our work, we get confirmation of the observation of Ref. [84] that the quark backreaction due to the unquenching of the Polyakov-loop potential links the chiral and deconfinement phase transitions also at small temperatures and large chemical potentials. Here, it is also relevant to recall that for the  $m_\sigma = 500$  MeV case, the CEP for the two flavor RQM model lies at the  $T_{\text{CEP}} = 36.2$  MeV and the  $\mu_{\text{CEP}} = 277.3$  MeV [67] in the absence of the Polyakov-loop effect. Thus, whatever be the form of Polyakov-loop potential when combined with the chiral physics, it generates a noteworthy upward shift of the CEP in the  $\mu - T$  plane.

Figure 6(a) depicts the phase diagram for the  $m_\sigma = 600$  MeV case. In comparison to the lower  $\sigma$  meson masses, the CEP in the Log PQM model shifts rightwards at  $T_{\text{CEP}} = 159.3$  MeV and  $\mu_{\text{CEP}} = 174.5$  MeV. The entire phase boundary for the Log PQMVT model becomes a crossover transition line. The position of the CEP for the Log RPQM model is found at  $T_{\text{CEP}} = 39.1$  MeV and  $\mu_{\text{CEP}} = 321.0$  MeV. In the PolyLog-gluon RPQM model with the  $T_0 \equiv T_0(\mu) = T_c^{\text{glue}}(\mu)$ , due to the effect of the quark backreaction, the CEP gets located at the

$T_{\text{CEP}} = 24.8$  MeV and the  $\mu_{\text{CEP}} = 318.9$  MeV. In comparison to the  $m_\sigma = 400$  and 500 MeV cases, here for the  $m_\sigma = 600$  MeV, we note that the  $T_{\text{CEP}}$  registers a smaller downwards shift of 14.3 MeV with respect to the Log RPQM model  $T_{\text{CEP}}$ .

Figure 6(b) presents the comparison of phase diagrams in the Log RPQM model for the different  $\sigma$  meson masses of 400, 500, 600, 616, and 700 MeV. The location of the CEP at  $T_{\text{CEP}} = 100.1$  MeV and  $\mu_{\text{CEP}} = 245.3$  MeV for the  $m_\sigma = 400$  MeV shifts slightly right to  $T_{\text{CEP}} = 94.1$  MeV and  $\mu_{\text{CEP}} = 270.6$  MeV for the  $m_\sigma = 500$  MeV. The CEP registers a significant rightward shift when the  $m_\sigma = 600$  MeV and gets located at  $T_{\text{CEP}} = 39.1$  MeV and  $\mu_{\text{CEP}} = 321.0$  MeV. For the  $m_\sigma \geq 616$  MeV, the entire phase boundary depicts a crossover transition. Two crossover transition lines for the  $m_\sigma = 616$  and 700 MeV have also been shown in the figure.

### C. Quarkyonic phase and its disappearance

One can define two pseudocritical temperatures, the  $T_c^\Phi$  and the  $T_c^{\bar{\Phi}}$ , for the deconfinement crossover transition of the fields  $\Phi$  and  $\bar{\Phi}$  by identifying the respective peaks in the temperature variations of the  $\frac{\partial \Phi}{\partial T}$  and  $\frac{\partial \bar{\Phi}}{\partial T}$ . Locus of the different  $T_c^\Phi$  and  $T_c^{\bar{\Phi}}$  at different chemical potentials gives the respective phase boundaries for the crossover transition for the fields  $\Phi$  and  $\bar{\Phi}$ . Apart from the phase boundaries for the chiral crossover transition, the Fig. 7(a) presents the plots of the deconfinement crossover transition phase boundaries also for the fields  $\Phi$  and  $\bar{\Phi}$ . Phase diagrams for the RPQM model with Poly, Log, and PolyLog-gluon forms of the Polyakov-loop potential with the constant  $T_0 = 208$  MeV have been plotted in the Fig. 7(a), while the corresponding plots when the parameter  $T_0$  has the chemical potential dependence, i.e.,  $T_0 \equiv T_0(\mu)$ , have been plotted in the Fig. 7(b).

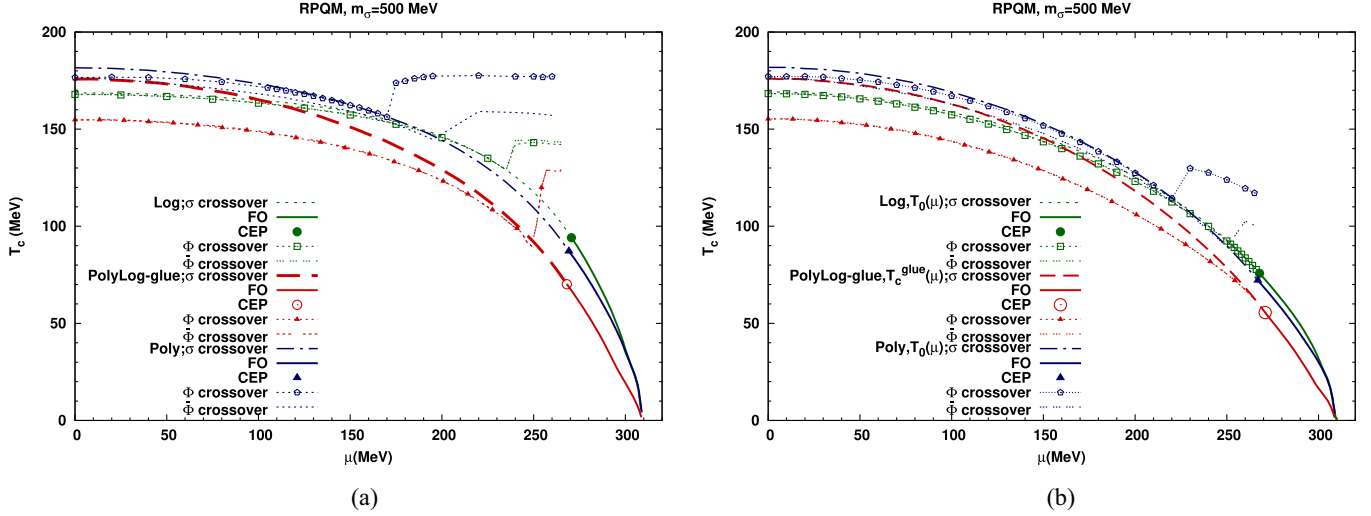


FIG. 7. Deconfinement and chiral transition phase boundaries for the Log, Poly, and PolyLog-gluon form of the Polyakov-loop potentials in the RPQM model (a) for the constant  $T_0 = 208$  MeV and (b) for the  $\mu$  dependent  $T_0 \equiv T_0(\mu) = T_c^{\text{glue}}(\mu)$ .

In the Fig. 7(a), when the  $\mu = 0$  to 130 MeV in the Poly RPQM model for the constant  $T_0$ , the deconfinement crossover transition line for the  $\bar{\Phi}$  lies below the corresponding line for the  $\Phi$ , and both of these lines get placed below the chiral crossover transition line, i.e.,  $T_c^{\bar{\Phi}} < T_c^{\Phi} < T_c^{\chi}$ . The  $\Phi$  crossover line, after remaining almost coincident with the chiral crossover line in the  $\mu = 130$ –170 MeV range, branches out of it, and the deconfinement transition temperature  $T_c^{\Phi}$  jumps to 173.8 MeV, while the  $T_c^{\chi} = 154.6$  MeV when the  $\mu$  becomes 175 MeV. Thus, we are getting a region in the phase diagram where the deconfinement crossover transition line for the field  $\Phi$  lies significantly above the chiral crossover line and the  $T_c^{\Phi} > T_c^{\chi}$ . The abovementioned portion of the phase diagram, where the chiral symmetry is restored but the quarks are still confined, has been identified as the quarkyonic phase in the literature [31,90–92]. Here in the Poly RPQM model, a significantly large region of the quarkyonic phase is obtained for the field  $\Phi$  as it starts early when the  $\mu \geq 175$  MeV. The  $\bar{\Phi}$  crossover line remains below the chiral transition line up till the  $\mu = 205$  MeV and crosses it between  $\mu = 205$ –210 MeV as the  $T_c^{\bar{\Phi}}$  jumps to 157.6 MeV, while the  $T_c^{\chi}$  stays at 139.1 MeV and the  $T_c^{\bar{\Phi}} > T_c^{\chi}$ . Here, the extent of the so-called quarkyonic phase for the field  $\bar{\Phi}$  is moderate as it starts from the  $\mu \geq 210$  MeV. When we consider the  $\mu$  dependence of the  $T_0 \equiv T_0(\mu)$  for the Poly RPQM model in the Fig. 7(b), the extent of quarkyonic phase for the  $\Phi$  and the  $\bar{\Phi}$ , is considerably reduced. The deconfinement transition phase boundary for the  $\Phi$  branches out of the chiral transition line for the  $\mu > 225$  MeV, while the corresponding line for the  $\bar{\Phi}$  forks out from the chiral crossover line for the  $\mu > 255$  MeV. Thus, the quarkyonic phase for the  $\Phi$  begins from the  $\mu > 225$  MeV, while it begins from the  $\mu > 255$  MeV for the  $\bar{\Phi}$ .

The two deconfinement crossover transition lines for the  $\Phi$  and  $\bar{\Phi}$  in the Log RPQM model are coincident in the Fig. 7(a). Lying below the chiral crossover transition line, these lines keeping a small temperature difference from it in the chemical potential range 0–220 MeV, get merged with it at the  $\mu = 220$  MeV and remain so up till  $\mu = 235$  MeV. Both of the deconfinement crossover lines fork out of the chiral crossover transition line together at  $\mu = 235$  MeV by registering a significant jump in the deconfinement crossover temperatures for the  $\Phi$  and  $\bar{\Phi}$  as the  $T_c^{\Phi}$  becomes 142.1 MeV and the  $T_c^{\bar{\Phi}}$  becomes 144.1 MeV at  $\mu = 240.0$  MeV, while the chiral crossover temperature remains at the  $T_c^{\chi} = 125.6$  MeV. Here in the Log RPQM model with the constant  $T_0$  case, one gets the simultaneous onset of the quarkyonic phase for both the fields  $\Phi$  and  $\bar{\Phi}$ , and its region is considerably smaller when compared to the Poly RPQM model as it starts from the chemical potential  $\mu > 240$  MeV. When we see the plots for the Log RPQM model with chemical potential dependent  $T_0(\mu)$  in the Fig. 7(b), we find that the two coincident  $\Phi$  and  $\bar{\Phi}$  deconfinement crossover transition lines do not fork out of the chiral crossover transition line at higher chemical potentials and remain merged with it. Thus, the quarkyonic phase disappears in the Log RPQM model for the chemical potential dependent  $T_0 \equiv T_0(\mu)$ .

For the PolyLog-gluon RPQM model in the Fig. 7(a) at the constant  $T_0$ , the deconfinement crossover transition phase boundaries for the  $\Phi$  and  $\bar{\Phi}$  are completely degenerate and get placed at lower temperatures than the chiral crossover transition line in the  $\mu = 0$  to 250 MeV range, i.e.,  $T_c^{\Phi} = T_c^{\bar{\Phi}} < T_c^{\chi}$ . The coincident deconfinement crossover lines are crossing the chiral transition phase boundary near the  $\mu = 250$  MeV and take a robust jump, such that the  $T_c^{\Phi} = T_c^{\bar{\Phi}} = 125.3$  MeV at the  $\mu = 255$  MeV, while

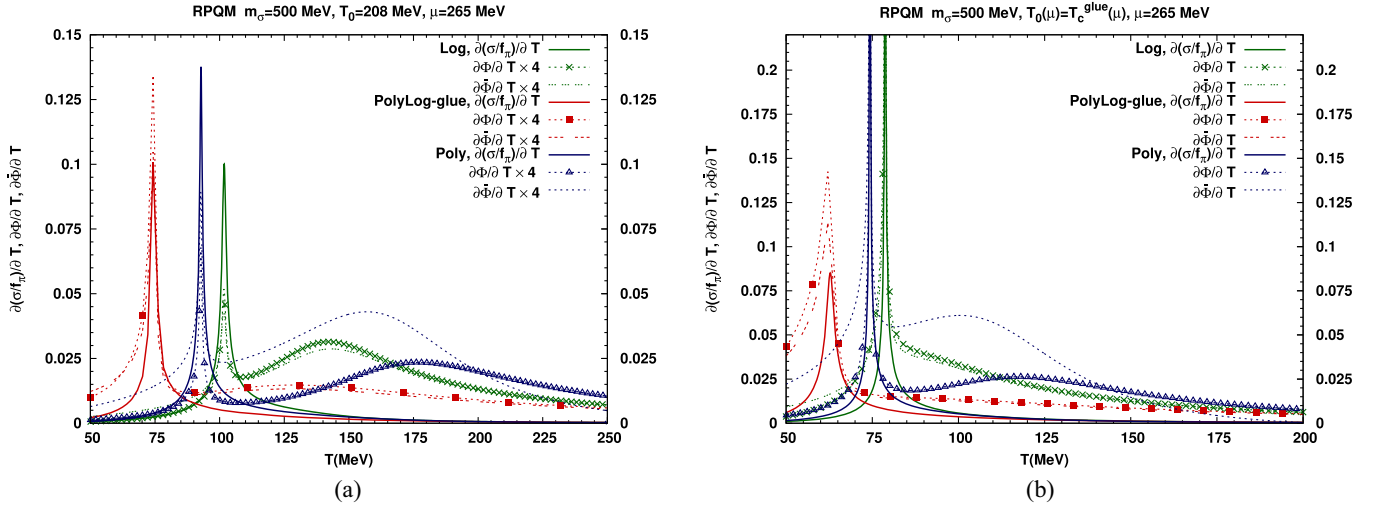


FIG. 8. The temperature variation of  $\frac{\partial(\sigma/f_\pi)}{\partial T}$ ,  $\frac{\partial\Phi}{\partial T}$  and  $\frac{\partial\bar{\Phi}}{\partial T}$  for the Log, Poly and PolyLog-gluon form of the Polyakov-loop potentials in the RPQM model at  $\mu = 265$  MeV, (a) for the constant  $T_0 = 208$  MeV, and (b) for the  $\mu$  dependent  $T_0 \equiv T_0(\mu) = T_c^{\text{glue}}(\mu)$ .

the  $T_c^\chi$  stays at 86.6 MeV. Thus, one gets the quarkyonic phase, and the region of its existence is found to be the smallest in the PolyLog-gluon RPQM model as it sets in for the  $\mu > 255$  MeV. When we examine the PolyLog-gluon RPQM model plot for the chemical potential dependent  $T_0 \equiv T_0(\mu) = T_c^{\text{glue}}(\mu)$  case, we do not find any region of quarkyonic phase as the degenerate deconfinement crossover lines completely merge with the chiral crossover transition line for  $\mu \geq 265$  MeV. Here, we recall that Schaefer *et al.* [77,85] have argued that the incidence of quarkyonic phase presents an unphysical scenario because the deconfinement temperature should be smaller or equal to the chiral transition temperature. Similar to our Log RPQM model finding, they have also reported the coincidence of the chiral and deconfinement transition lines for the entire phase diagram when the parameter  $T_0$  is taken as the  $\mu$  dependent  $T_0(\mu)$ . Thus, the quarkyonic phase looks like an artifact of the model.

In order to see how the deconfinement transition temperatures  $T_c^\Phi$  and  $T_c^{\bar{\Phi}}$  in one model setting differ from the corresponding chiral transition temperature  $T_c^\chi$  in the region of quarkyonic phase, the temperature variations of the  $\frac{\partial(\sigma/f_\pi)}{\partial T}$ ,  $\frac{\partial\Phi}{\partial T}$ , and  $\frac{\partial\bar{\Phi}}{\partial T}$ , have been plotted for the  $\mu = 265$  MeV, respectively, in the Fig. 8(a) for the constant  $T_0$  case and in the Fig. 8(b) for the  $\mu$  dependent case  $T_0 \equiv T_0(\mu)$ . When the double peak structure emerges in the temperature variations of the  $\frac{\partial\Phi}{\partial T}$  and the  $\frac{\partial\bar{\Phi}}{\partial T}$  at higher chemical potentials, one identifies the quarkyonic phase. Since the chiral transition dynamics is the driver of the first peak formation at a lower temperature, its location coincides with the chiral crossover temperature  $T_c^\chi$ . The second peak gets located at a higher temperature respectively for the  $\frac{\partial\Phi}{\partial T}$  and the  $\frac{\partial\bar{\Phi}}{\partial T}$  temperature variations, and one gets  $T_c^\Phi > T_c^\chi$  and  $T_c^{\bar{\Phi}} > T_c^\chi$ . The  $\frac{\partial\Phi}{\partial T}$  and  $\frac{\partial\bar{\Phi}}{\partial T}$  temperature variations in the Fig. 8(a) show the clear structure of the double peaks in the respective red,

green, and blue line plots for the PolyLog-gluon, Log, and Poly RPQM model, where the quarkyonic phase exists for the constant  $T_0$  case. The first peak of the preceding plots coincide with the peak of the  $\frac{\partial(\sigma/f_\pi)}{\partial T}$  temperature variations for the corresponding model. The temperature variations of the  $\frac{\partial\Phi}{\partial T}$  and  $\frac{\partial\bar{\Phi}}{\partial T}$  in the Fig. 8(b), do not show any double peak structure in the respective red and green line plots of the PolyLog-gluon and the Log RPQM model because the quarkyonic phase disappears for the chemical potential dependent  $T_0 \equiv T_0(\mu)$ . The corresponding blue line plots for the Poly RPQM model, show the distinct double peaks due the presence of the quarkyonic phase.

#### D. Pressure, entropy density, energy density, and interaction measure

The thermodynamic observables pressure, entropy, energy density, and interaction measure are sensitive to the QCD phase transition. Considering the PolyLog-gluon ansatz for the Polyakov-loop potential, the abovementioned observables have been computed and compared to see how the PQM model results are changed by the quark one-loop vacuum correction in the on-shell parametrization of the RPQM model versus the curvature mass parametrization of the PQMVT model. It is also worthwhile to compare, how the thermodynamic observables are influenced when one takes different form of the Polyakov-loop potential namely the Log, Log-gluon, or PolyLog-gluon for combining it with the consistent chiral physics of the RPQM model.

The negative grand potential gives us the pressure,

$$P(T, \mu) = -\Omega_{MF}(T, \mu), \quad (52)$$

the pressure in vacuum has been normalized to zero, i.e.,  $P(0, 0) = 0$ . When the  $\mu = 0$ , the ideal gas Stefan-Boltzmann limit (SB) pressure is defined as

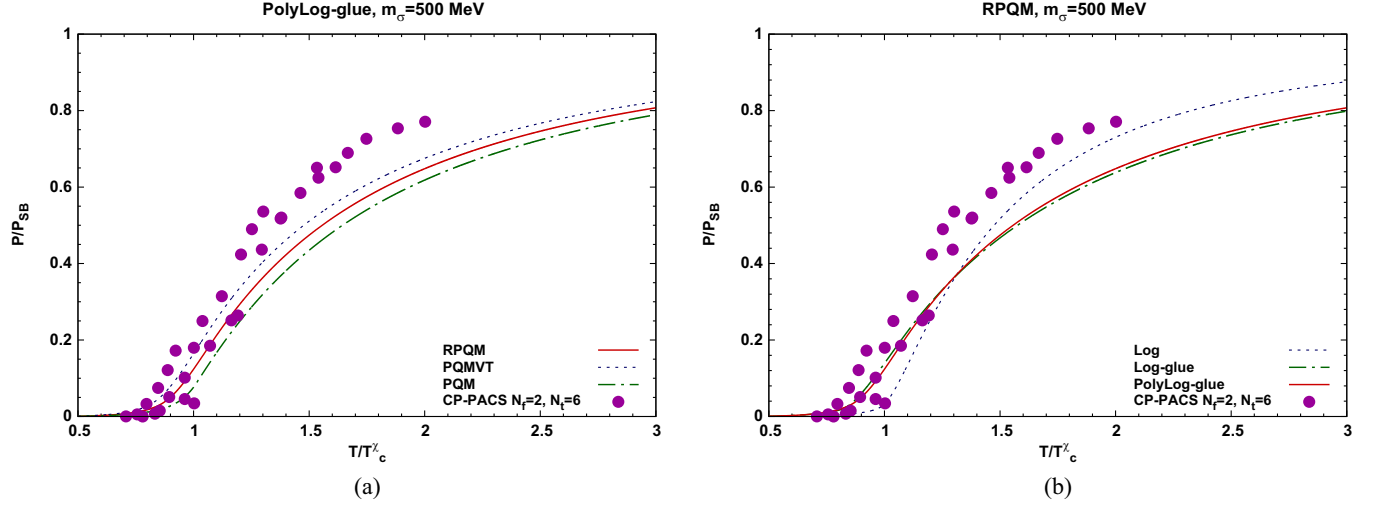


FIG. 9. Reduced temperature scale variation of the pressure normalized to its Stefan-Boltzmann limit for the (a) RPQM, PQMVT, and PQM model with the PolyLog-gluon form of the Polyakov-loop potential, (b) RPQM model with the Log, Log-gluon, and PolyLog-gluon form of the Polyakov-loop potential. The two flavor LQCD data of the pressure have been taken from the Ref. [6].

$$\frac{P_{SB}}{T^4} = (N_c^2 - 1) \frac{\pi^2}{45} + N_c N_f \frac{7\pi^2}{180}. \quad (53)$$

Figure 9(a) presents the comparison of the PQM, RPQM, and PQMVT model plots of the normalized pressure ( $\frac{P}{P_{SB}}$ ) on the reduced temperature scale when the  $m_\sigma = 500$  MeV and the PolyLog-gluon form of the unquenched Polyakov-loop potential has been taken. The two flavor lattice QCD data of pressure normalized with the corresponding SB limit (on the discretized space-time) [6] have also been presented for the comparison. The normalized pressure for the RPQM model shows a decent agreement with the lattice data in the range 0.7 to 1.25 of the  $T_c^\chi$ . The quark one-loop

vacuum correction leads to the increased pressure and the largest increase of pressure is noticed in the PQMVT model. In the Fig. 9(b), one can see that the rise of the pressure in the Log RPQM model near the chiral transition temperature gets significantly modified in the Log-gluon and PolyLog-gluon RPQM model due to the quark backreaction and unquenching of the Polyakov-loop potential. The rise in the pressure is caused by the melting of the constituent quark masses, and it saturates near 80% of the SB limit.

The entropy density  $s$ , energy density  $\epsilon$  and interaction measure  $\Delta$  are defined as

$$s = -\frac{\partial\Omega}{\partial T}, \quad (54)$$

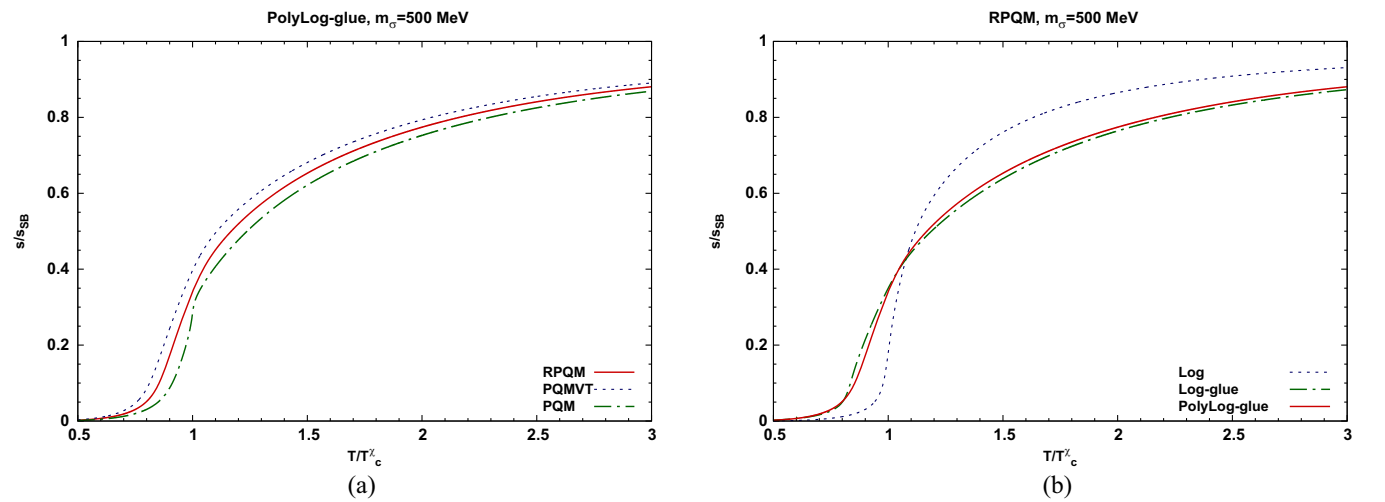


FIG. 10. Reduced temperature scale variation of the entropy density normalized to its Stefan-Boltzmann limit for the (a) RPQM, PQMVT, and PQM model with the PolyLog-gluon form of the Polyakov-loop potential, (b) RPQM model with the Log, Log-gluon, and PolyLog-gluon form of the Polyakov-loop potential.

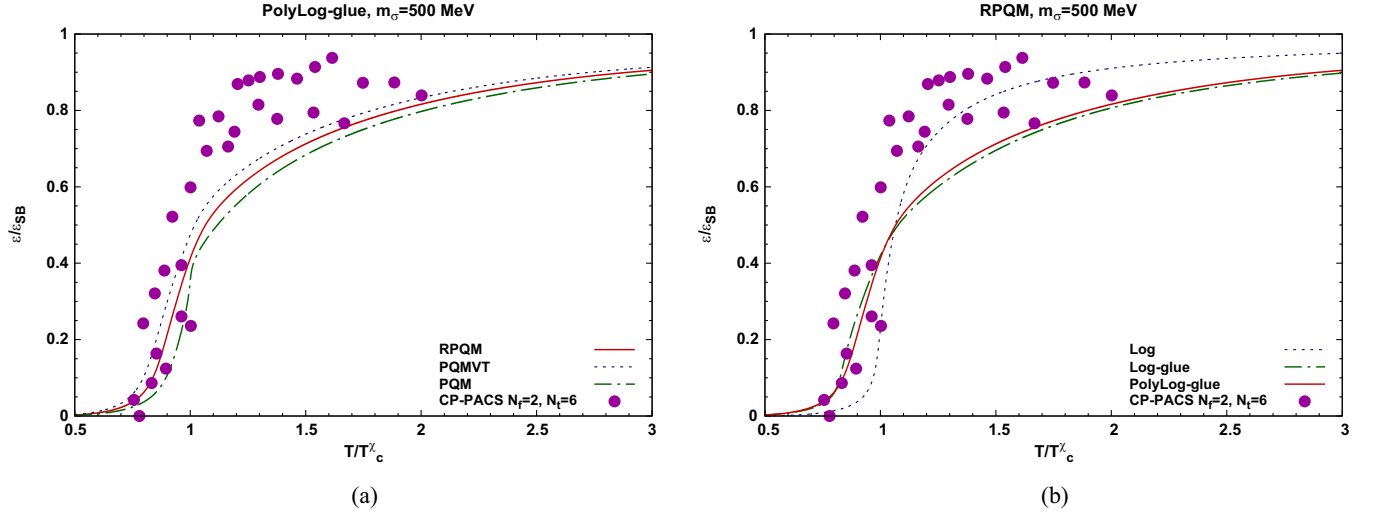


FIG. 11. Reduced temperature scale variation of the energy density normalized to its Stefan-Boltzmann limit for the (a) RPQM, PQMVT, and PQM model with the PolyLog-gluon form of the Polyakov-loop potential, (b) RPQM model with the Log, Log-gluon, and PolyLog-gluon form of the Polyakov-loop potential. The two flavor lattice QCD data of the energy density have been taken from the Ref. [6].

$$\epsilon = -P + Ts, \quad (55)$$

$$\Delta = \epsilon - 3P. \quad (56)$$

Figure 10(a) presents the reduced temperature scale plot of the entropy density normalized to its SB limit. Similar to the pressure, the quark one-loop vacuum correction leads to the increased entropy density  $s/s_{SB}$ . When the entropy density plot for the PolyLog-gluon RPQM and PQMVT model are compared with that of the PQM Model, one gets largest entropy density increase in the PQMVT model, while the corresponding increase in the

RPQM model is moderate. Even though the smoothing effect of the quark backreaction is present in the PolyLog-gluon PQM model, the entropy density shows a small kink at the chiral transition temperature ( $T/T_c = 1$ ). This kink gets smoothed out in the RPQM and PQMVT plots. The quark backreaction in the Log-gluon and PolyLog-gluon RPQM model causes a significant smoothing change in the rapidly increasing entropy density plot of the Log RPQM model in the Fig. 10(b). The plots of the normalized energy density on the reduced temperature scale in the Figs. 11(a) and 11(b) show the same trend that we get for the normalized entropy density respectively in the Figs. 10(a) and 10(b). The energy density plot for the

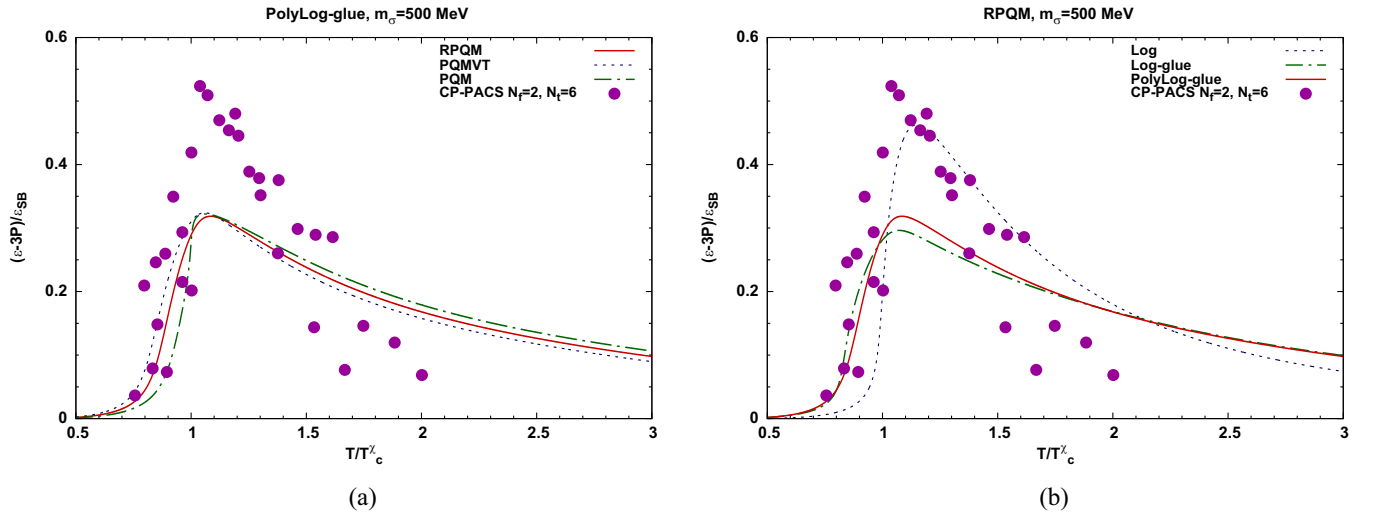


FIG. 12. Reduced temperature scale variation of the interaction measure normalized to the Stefan-Boltzmann limit of energy density for the (a) RPQM, PQMVT, and PQM model with the PolyLog-gluon form of the Polyakov-loop potential, (b) RPQM model with the Log, Log-gluon, and PolyLog-gluon form of the Polyakov-loop potential. The two flavor lattice QCD data of the interaction measure have been taken from the Ref. [6].

PolyLog-gluon RPQM model shows better agreement with the lattice QCD data [6] in the temperature range  $(0.7-1.1)T_c^\chi$  and  $(1.6-2.1)T_c^\chi$ .

Figure 12(a), shows the plots of the normalized interaction measure  $\Delta/\epsilon_{\overline{\text{SB}}}$  in the RPQM, PQMVT, and PQM model having the PolyLog-gluon form for the Polyakov-loop potential. The peak of the RPQM model plot stands a little right to that of the PQMVT and PQM model. The RPQM model plot agrees well with the lattice QCD data points up to  $T \sim T_c^\chi$  and a point near  $1.4T_c^\chi$ . Figure 12(b) presents the normalized interaction measure  $\Delta/\epsilon_{\overline{\text{SB}}}$  plot for the RPQM model using Log, Log-gluon, and PolyLog-gluon forms for the Polyakov-loop potential. Several lattice data points at the peak of the interaction measure lie on the line depicting the Log RPQM model result.

### E. Specific heat and speed of sound

The specific heat capacity at constant volume is defined by

$$C_V = \left. \frac{\partial \epsilon}{\partial T} \right|_V = -T \left. \frac{\partial^2 \Omega}{\partial T^2} \right|_V. \quad (57)$$

Figure 13(a) shows the variation of the normalized specific heat capacity at  $\mu = 0$  as a function of the reduced temperature when the PolyLog-gluon form has been taken for the Polyakov-loop potential in the RPQM, PQMVT, and PQM model. The highest and sharpest PQM model specific heat peak at the  $T_c^\chi$  gets significantly reduced and smoothed out in the temperature range  $(0.7-1.2)T_c^\chi$  due to the quark one-loop vacuum fluctuations in the PQMVT and RPQM model. The very sharp and high specific heat peak at the  $T_c^\chi$  for the Log RPQM model in the Fig. 13(b) becomes quite smooth, reduced, and round due to the

robust effect of the quark backreaction when the Log-gluon and the PolyLog-gluon form has been taken for the unquenching of the Polyakov-loop potential in the RPQM model. We point out that the two peak structure in the Log-gluon RPQM model plot for the specific heat is the consequence of the fact that the temperature variation of the chiral order parameter has two peaks as one can see in the Fig. 4(a). The specific heat plots for all the cases approach the corresponding SB-limit at high temperatures. Since the gluon degrees of freedom contribute differently [78], the specific heat plot for the Log RPQM model in the Fig. 13(b) does not merge completely with the Log-gluon and PolyLog-gluon RPQM model plots even when  $T = 3T_c^\chi$ .

The speed of sound is fundamental property of the strongly interacting medium. The square of the speed of sound at constant entropy density is defined as

$$C_s^2 = \left. \frac{\partial P}{\partial \epsilon} \right|_s = \left. \frac{\partial P}{\partial T} \right|_V / \left. \frac{\partial \epsilon}{\partial T} \right|_V = \frac{s}{C_V}. \quad (58)$$

The speed of sound and the ratio  $P/\epsilon$  have been plotted in the Fig. 14 on the reduced temperature scale. The  $C_s^2$  is very close to the  $P/\epsilon$  for the  $T < 0.7T_c^\chi$ . While approaching its ideal gas limit of  $1/3$  for the  $T > 2.5T_c^\chi$ , the  $C_s^2$  comes close to the  $P/\epsilon$  again. Similar to the results of Refs. [46,47], the  $C_s^2$  plot lies sufficiently above the  $P/\epsilon$  plot for the temperature interval  $0.7T_c^\chi < T < 2.5T_c^\chi$  except near the  $T_c^\chi$ . The very sharp and a relatively less sharp dip noticed at the  $T_c^\chi$ , respectively, in the  $C_s^2$  and the  $P/\epsilon$  plot for the PolyLog-gluon PQM model in the Fig. 14(a), becomes very smooth and moderately smooth for the respective cases of the PQMVT and RPQM model. In the PolyLog-gluon RPQM model, the speed of sound  $C_s^2$  plot shows a better agreement with the lattice QCD data around the  $T_c^\chi$  and the minimum value

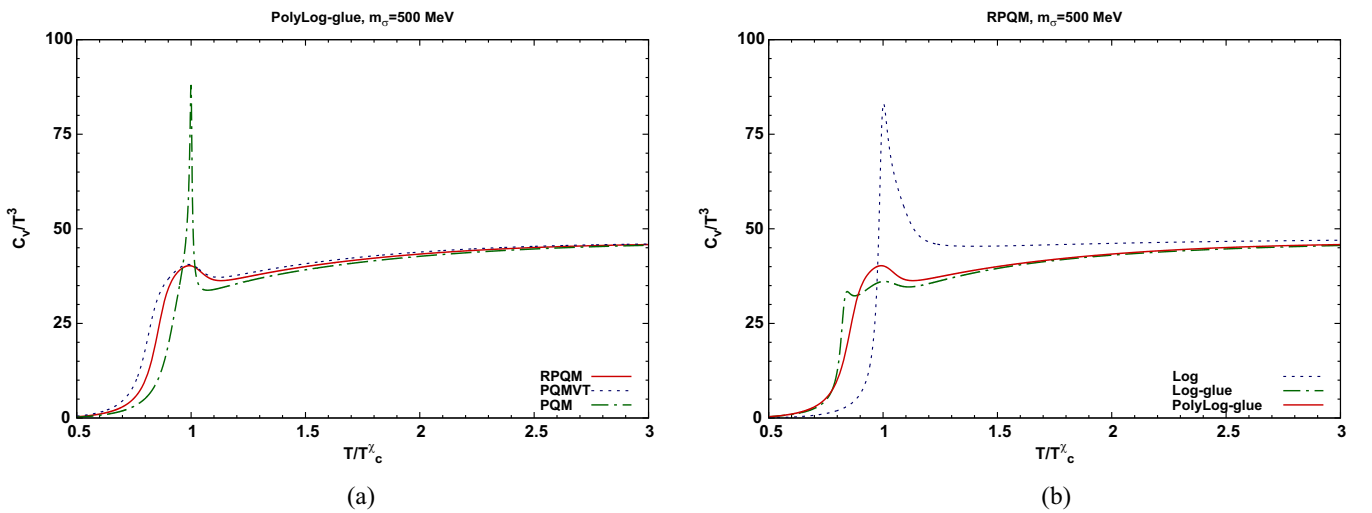


FIG. 13. Reduced temperature scale variation of the specific heat at constant volume normalized with  $T^3$  for the (a) RPQM, PQMVT, and PQM model with the PolyLog-gluon form of the Polyakov-loop potential, (b) RPQM model with the Log, Log-gluon, and PolyLog-gluon form of the Polyakov-loop potential.

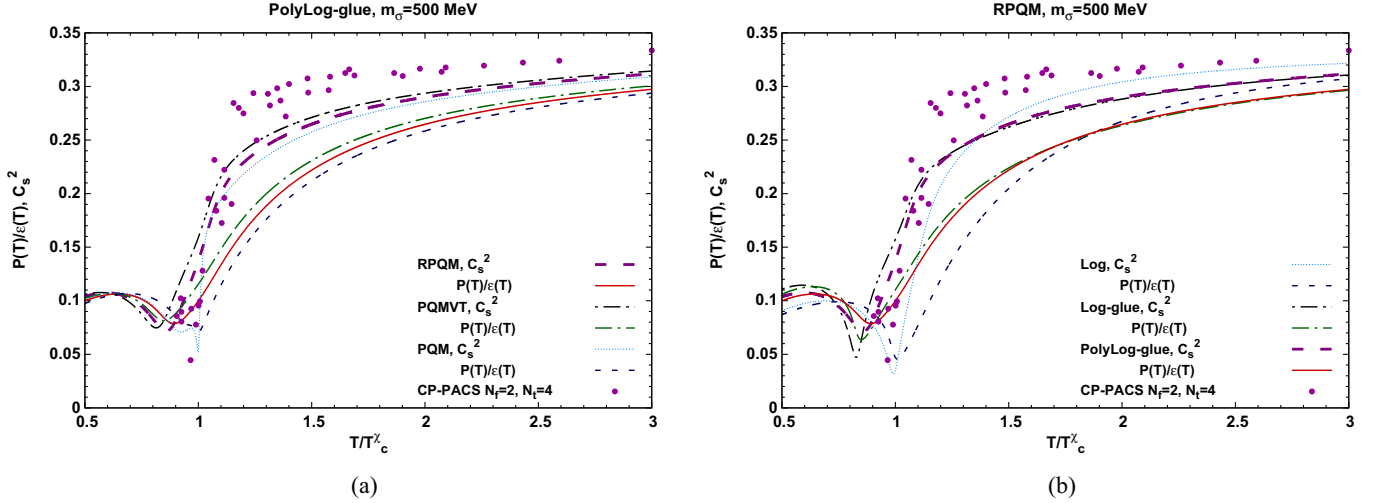


FIG. 14. Reduced temperature scale variation of the square of speed of sound and the ratio of pressure with energy density for the (a) RPQM, PQMVT, and PQM model with the PolyLog-gluon form of the Polyakov-loop potential, (b) RPQM model with the Log, Log-gluon, and PolyLog-gluon form of the Polyakov-loop potential. The two flavor lattice QCD data of the  $C_s^2$  have been taken from the Ref. [6].

0.078 for the ratio  $P/\epsilon$  is closest to the corresponding minimum value of 0.075 obtained from the lattice QCD in Ref. [14]. The Fig. 14(b) shows that the sharp  $C_s^2$  and  $P/\epsilon$  temperature variations for the Log RPQM model becomes quite smooth due to the quark backreaction in the Log-gluon and the PolyLog-gluon RPQM model, where the Polyakov-loop potential is unquenched. The Log RPQM model plot for the speed of sound  $C_s^2$ , lies closest to the lattice QCD data points at higher temperatures ( $T > 1.4T_c^\chi$ ). Similar to the findings of the Refs. [46,47], the  $C_s^2$  value is found to be less than 0.1 below the  $0.5T_c^\chi$  (not shown in the figure) in the all of our model results. This stands in contrast to the results of the Ref. [93], where a confinement model has been applied and the value of  $C_s^2 \sim 0.2$  in the vicinity of  $0.5T_c^\chi$  and  $C_s^2 \sim 0.15$  near the  $T_c^\chi$ .

## VI. SUMMARY AND CONCLUSION

Computing the phase diagrams and the thermodynamic quantities for the PQM, PQMVT, and RPQM model, we have compared how the quark one-loop vacuum correction in combination of the Polyakov-loop potential influences the dynamics of both the chiral as well as the confinement-deconfinement transition. Taking a different parametric form for the Polyakov-loop potential with/without the quark backreaction and the  $\mu$  dependence of the parameter  $T_0$ , we have also made a detailed comparison of how the chiral and Polyakov-loop condensates, their derivatives, phase diagrams, and the thermodynamic quantities get affected in the RPQM model, which has the exact chiral effective potential. The results obtained for the different thermodynamic quantities have also been compared with the available lattice QCD data.

The sharp temperature variation of the chiral condensate and its temperature derivative in the PQM model for the  $\mu = 0$  and  $m_\sigma = 500$  MeV become excessively smooth in the PQMVT model, while the corresponding smoothness turns out to be moderate when the effect of the quark one-loop vacuum correction is computed using the exact on-shell renormalized RPQM model. The deconfinement crossover transition occurs earlier than the chiral transition, i.e.,  $T_c^\Phi < T_c^\chi$ , except for the cases of the PolyLog-gluon PQM and the Log RPQM model, where the  $T_c^\Phi \sim T_c^\chi$ . The presence of the quark backreaction (represented by the glue form of the Polyakov-loop potential) in all the three chiral models generates a significant smoothing effect on the temperature variations of the chiral condensate, the Polyakov-loop condensate, and their derivatives. The combined effect of the quark backreaction and the one-loop vacuum correction for the PolyLog-gluon PQMVT model generates the highest separation of the  $(T_c^\chi - T_c^\Phi) = 30.2$  MeV between the deconfinement and the chiral crossover transition, while the corresponding separation generated for the PolyLog-gluon RPQM model is  $(T_c^\chi - T_c^\Phi) = 21.0$  MeV.

The phase boundary for the RPQM model stands closer to the PQM model phase boundary when compared to that of the PQMVT model. Since the Log PQMVT model generates excessively smooth chiral transition similar to the earlier findings [46–48,50,51,67], the critical end point (CEP) respectively for the  $m_\sigma = 400$  and 500 MeV cases gets located at the  $(T_{\text{CEP}} = 94.77$  MeV,  $\mu_{\text{CEP}} = 267.2$  MeV) and the  $(T_{\text{CEP}} = 78.0$  MeV,  $\mu_{\text{CEP}} = 295.9$  MeV) positions in the right lower corner of the phase diagram. The on-shell renormalized Log-RPQM model gives rise to a relatively moderate smoothing effect on the chiral transition; hence, the CEP gets located higher up in the phase

diagram respectively at the ( $T_{\text{CEP}} = 100.1$  MeV,  $\mu_{\text{CEP}} = 245.3$  MeV) and the ( $T_{\text{CEP}} = 94.1$  MeV,  $\mu_{\text{CEP}} = 270.6$  MeV) for the  $m_\sigma = 400$  and 500 MeV.

When compared to the CEP in the Log RPQM model for the  $m_\sigma = 500$  MeV, the CEP for the PolyLog-gluon RPQM model with the  $T_0 \equiv T_0(\mu)$ , shifts down in temperature by 38.5 MeV due to the significant smoothing effect of the quark backreaction in the temperature direction and gets located at the  $T_{\text{CEP}} = 55.6$  MeV, while the chemical potential registers a negligible shift as the  $\mu_{\text{CEP}} = 270.9$  MeV. Due to the above effect, the curvature of the phase transition line increases significantly for all the cases where the unquenching of the Polyakov-loop potential has been considered. In our work, the observation of the Ref. [84] is confirmed that the unquenching of the Polyakov-loop potential links the chiral and deconfinement phase transitions at all temperatures and chemical potentials. Comparing the results of the Polyakov-loop enhanced calculations with the two flavor RQM model results [67] where the effect of Polyakov-loop is absent, we note that the presence of Polyakov-loop potential either in the Log or in the PolyLog-gluon form in the RPQM model leads to significant upward shift of the CEP in the  $\mu - T$  plane.

The occurrence of the so-called quarkyonic phase, where the chiral symmetry is restored but the quarks and antiquarks are confined, depends on the form taken for the Polyakov loop potential. It occurs in a large region of the phase diagram for the Poly RPQM model, while its region gets reduced for the Log RPQM model. Its region gets significantly reduced by the quark back-reaction in the unquenched Polyakov-loop potential. It altogether disappears when the parameter  $T_0$  becomes chemical potential dependent i.e.,  $T_0 \equiv T_0(\mu)$  in the Log or the PolyLog-gluon form of the Polyakov-loop potential in the RPQM model, while it occurs with a significantly reduced extent for the corresponding case of the polynomial form of the Polyakov-loop potential in the RPQM model.

The thermodynamic quantities namely the pressure, entropy density, energy density, interaction measure, specific heat, the speed of sound, and the  $P/\epsilon$  ratio have been computed for the  $\mu = 0$  and the  $m_\sigma = 500$  MeV. As expected, their variations in the PQMVT model are smoother than that of the RPQM Model. The sharp reduced temperature scale variation in the Log RPQM model becomes quite smooth due to the quark backreaction in the Log-gluon and the PolyLog-gluon RPQM model. Comparing the results with the available lattice QCD data, we find that near the chiral transition  $(0.7-1.2)T_c^\chi$ , the PolyLog-gluon RPQM model results for all the thermodynamic quantities are in the best agreement with the lattice QCD results. The Log RPQM model results are close to the lattice QCD results at higher temperatures. In the PolyLog-gluon RPQM model, the minimum value 0.078 for the ratio  $P/\epsilon$  is closest to the corresponding minimum value of 0.075 obtained from the lattice QCD in Ref. [14].

## ACKNOWLEDGMENTS

The authors would like to thank Shinji Ejiri for providing the lattice data of CP-PACS Collaboration [6].

## APPENDIX A: THE QMVT PARAMETER FIXING

The tree level expression of the curvature masses of mesons for the QM model are given by the mass matrix evaluated in Ref. [22]. In this work, the above mass matrix is renamed as  $(m_{\alpha,ab}^m)^2$ , where superscript  $m$  stands for the contribution of the pure mesonic potential. In the QMVT model, the meson curvature masses get modified by the quark one-loop vacuum contribution. The total expression of the meson curvature masses in the QMVT model is written as

$$m_{\alpha,ab}^2 = (m_{\alpha,ab}^m)^2 + (\delta m_{\alpha,ab}^v)^2, \quad (\text{A1})$$

where  $\alpha = s, p$ ; “s” stands for the scalar and “p” stands for the pseudoscalar mesons and  $a, b = 0, 1, 2, 3$ .  $m_{s,00}^2 \equiv m_\sigma^2$ ;  $m_{s,11}^2 = m_{s,22}^2 = m_{s,33}^2 \equiv m_{a_0}^2$  and  $m_{p,00}^2 \equiv m_\eta^2$ ;  $m_{p,11}^2 = m_{p,22}^2 = m_{p,33}^2 \equiv m_\pi^2$ . The  $(m_{\alpha,ab}^m)^2$  and  $(\delta m_{\alpha,ab}^v)^2$  are defined in the similar fashion. The expressions of the curvature masses  $(m_{\alpha,ab}^m)^2$  are presented in the Table V. Superscript “v” stands for the quark/antiquark vacuum contribution to the curvature masses. It is written as

$$\begin{aligned} (\delta m_{\alpha,ab}^v)^2 &= \left. \frac{\partial^2 \Omega_{q\bar{q}}^{\text{vac}}}{\partial \xi_{\alpha,a} \partial \xi_{\alpha,b}} \right|_{\text{min}}, \\ &= \sum_{q=u,d} \frac{2N_c}{(4\pi)^2} \left[ \{m_{q,aa}^2 m_{q,ab}^2 + m_q^2 m_{q,aab}^2\} \right. \\ &\quad \left. \left\{ 1 + \ln \left( \frac{\Lambda^2}{m_q^2} \right) \right\} - m_{q,aa}^2 m_{q,ab}^2 \right], \end{aligned} \quad (\text{A2})$$

where  $m_{q,aa}^2 = \frac{\partial m_q^2}{\partial \xi_{\alpha,a}^2}$  and  $m_{q,aab}^2 = \frac{\partial m_{q,aa}^2}{\partial \xi_{\alpha,b}^2}$ . The  $\xi$  fields are defined in the Eq. (7). When one computes the second derivative of the Eq. (44) for the quark contribution, the full dependence of all the scalar and pseudoscalar meson fields, cf. Eq. (8), in the quark masses has to be considered. The resulting quark mass matrix is diagonalized similar to the three flavor case given in Ref. [41]. In all the quark mass

TABLE V. Expressions of the curvature masses  $(m_{\alpha,ab}^m)^2$  are calculated from the second derivative of the pure mesonic potential as has been evaluated in Ref. [22].

$(m_{\alpha,ab}^m)^2$		Meson mass found from the pure mesonic potential
$(m_{s,00}^m)^2$	$(m_\sigma^m)^2$	$m^2 - c + 3(\lambda_1 + \frac{\lambda_2}{2})\bar{\sigma}^2$ ,
$(m_{s,11}^m)^2$	$(m_{a_0}^m)^2$	$m^2 + c + (\lambda_1 + \frac{3\lambda_2}{2})\bar{\sigma}^2$ ,
$(m_{p,00}^m)^2$	$(m_\eta^m)^2$	$m^2 + c + (\lambda_1 + \frac{\lambda_2}{2})\bar{\sigma}^2$ ,
$(m_{p,11}^m)^2$	$(m_\pi^m)^2$	$m^2 - c + (\lambda_1 + \frac{\lambda_2}{2})\bar{\sigma}^2$ ,

TABLE VI. Squared quark mass derivatives with respect to the meson fields evaluated at the minimum. The last two columns present the first and second derivative of the squared quark mass summed over two quark flavor. The “s” stands for the scalar and “p” stands for the pseudoscalar mesons and  $a, b = 0, 1, 2, 3$ .

$s/p$	$a$	$b$	$m_{q,aa}^2 m_{q,ab}^2 / g^4$	$m_{q,aab}^2 / g^2$
$s$	0	0	$\frac{1}{2}\bar{\sigma}^2$	1
$s$	1	1	$\frac{1}{2}\bar{\sigma}^2$	1
$p$	0	0	0	1
$p$	1	1	0	1

derivatives with respect to the meson fields, the meson fields are replaced by the nonvanishing vacuum expectation value  $\bar{\sigma}$ , and the final values are collected in the Table VI.

Using the Table VI in the Eq. (A2), we get vacuum contributions of meson masses as

$$(\delta m_\sigma^v)^2 \equiv (\delta m_{s,00}^v)^2 = \frac{N_c g^4 \bar{\sigma}^2}{2(4\pi)^2} \left[ 1 + 3 \ln \left( \frac{\Lambda^2}{m_q^2} \right) \right], \quad (\text{A3})$$

$$(\delta m_{a_0}^v)^2 \equiv (\delta m_{s,11}^v)^2 = \frac{N_c g^4 \bar{\sigma}^2}{2(4\pi)^2} \left[ 1 + 3 \ln \left( \frac{\Lambda^2}{m_q^2} \right) \right], \quad (\text{A4})$$

$$(\delta m_\eta^v)^2 \equiv (\delta m_{p,00}^v)^2 = \frac{N_c g^4 \bar{\sigma}^2}{2(4\pi)^2} \left[ 1 + \ln \left( \frac{\Lambda^2}{m_q^2} \right) \right], \quad (\text{A5})$$

$$(\delta m_\pi^v)^2 \equiv (\delta m_{p,11}^v)^2 = \frac{N_c g^4 \bar{\sigma}^2}{2(4\pi)^2} \left[ 1 + \ln \left( \frac{\Lambda^2}{m_q^2} \right) \right]. \quad (\text{A6})$$

We get  $(m_\sigma^m)^2, (m_\eta^m)^2, (m_{a_0}^m)^2$ , and  $(m_\pi^m)^2$  after substitution of the Eqs. (A3)–(A6) into the Eq. (A1) as

$$(m_\sigma^m)^2 = m_\sigma^2 - \frac{N_c g^4 \bar{\sigma}^2}{2(4\pi)^2} \left[ 1 + 3 \ln \left( \frac{\Lambda^2}{m_q^2} \right) \right], \quad (\text{A7})$$

$$(m_{a_0}^m)^2 = m_{a_0}^2 - \frac{N_c g^4 \bar{\sigma}^2}{2(4\pi)^2} \left[ 1 + 3 \ln \left( \frac{\Lambda^2}{m_q^2} \right) \right], \quad (\text{A8})$$

$$(m_\eta^m)^2 = m_\eta^2 - \frac{N_c g^4 \bar{\sigma}^2}{2(4\pi)^2} \left[ 1 + \ln \left( \frac{\Lambda^2}{m_q^2} \right) \right], \quad (\text{A9})$$

$$(m_\pi^m)^2 = m_\pi^2 - \frac{N_c g^4 \bar{\sigma}^2}{2(4\pi)^2} \left[ 1 + \ln \left( \frac{\Lambda^2}{m_q^2} \right) \right]. \quad (\text{A10})$$

The parameters in vacuum are obtained as

$$\lambda_1 = \frac{(m_\sigma^m)^2 + (m_\eta^m)^2 - (m_{a_0}^m)^2 - (m_\pi^m)^2}{2f_\pi^2}, \quad (\text{A11})$$

$$\lambda_2 = \frac{(m_{a_0}^m)^2 - (m_\eta^m)^2}{f_\pi^2}, \quad (\text{A12})$$

$$m^2 = (m_\pi^m)^2 + \frac{(m_\eta^m)^2 - (m_\sigma^m)^2}{2}, \quad (\text{A13})$$

$$c = \frac{(m_\eta^m)^2 - (m_\pi^m)^2}{2}. \quad (\text{A14})$$

We get the parameters of the QMVT model on substitution of the Eqs. (A7)–(A10) into the Eqs. (A11)–(A14).  $\lambda_1, c$  of the QMVT model are same with respect to the  $\lambda_1, c$  of the QM model. We observe change in  $\lambda_2$  and  $m^2$  as

$$\lambda_2 = \lambda_{2s} - \frac{N_c g^4}{(4\pi)^2} \ln \left( \frac{4\Lambda^2}{g^2 f_\pi^2} \right), \quad (\text{A15})$$

$$m^2 = m_s^2 - \frac{N_c g^4 f_\pi^2}{2(4\pi)^2}, \quad (\text{A16})$$

where  $\lambda_{2s}$  and  $m_s^2$  are same old  $\lambda_2$  and  $m^2$  parameters of the QM model. Putting the value of the new parameters  $\lambda_2$  and  $m^2$  in Eq. (A10), one can write the expression of pion mass independent of renormalization scale as

$$m_\pi^2 = m_s^2 - \frac{N_c g^4}{2(4\pi)^2} (f_\pi^2 - \bar{\sigma}^2) - c + \left( \lambda_1 + \frac{\lambda_{2s}}{2} \right) \bar{\sigma}^2 + \frac{N_c g^4}{2(4\pi)^2} \log \left( \frac{f_\pi^2}{\bar{\sigma}^2} \right) \bar{\sigma}^2. \quad (\text{A17})$$

## APPENDIX B: FIXING OF THE PARAMETERS IN THE RQM MODEL

In the RQM model, the divergence of the first term of the Eq. (37) [as rewritten in the Eq. (44)] is removed by the renormalization of its parameters. This appendix presents the relation between the physical quantities and the parameters of the Lagrangian (4) using the  $\overline{\text{MS}}$  and on-shell renormalization schemes [67,94]. One introduces the counterterms  $\delta m^2, \delta g^2, \delta \lambda_1, \delta \lambda_2, \delta c$ , and  $\delta h$  for the parameters and the wave function/field counterterms  $\delta Z_\sigma, \delta Z_{a_0}, \delta Z_\eta, \delta Z_\pi, \delta Z_\psi$ , and  $\delta Z_{\bar{\sigma}}$  in the Lagrangian (4) to define the renormalized fields and couplings,

$$\sigma_b = \sqrt{Z_\sigma} \sigma, \quad \eta_b = \sqrt{Z_\eta} \eta, \quad a_{0b}^i = \sqrt{Z_{a_0}} a_0 \quad (\text{B1})$$

$$\pi_b^i = \sqrt{Z_\pi} \pi, \quad \psi_b = \sqrt{Z_\psi} \psi, \quad m_b^2 = Z_m m^2 \quad (\text{B2})$$

$$\lambda_{1b} = Z_{\lambda_1} \lambda_1, \quad \lambda_{2b} = Z_{\lambda_2} \lambda_2, \quad g_b = \sqrt{Z_g} g \quad (\text{B3})$$

$$h_b = Z_h h, \quad c_b = Z_c c, \quad \bar{\sigma}_b = \sqrt{Z_{\bar{\sigma}}} \bar{\sigma} \quad (\text{B4})$$

where  $Z_{(\sigma, a_0, \eta, \pi, \psi, \bar{\sigma})} = 1 + \delta Z_{(\sigma, a_0, \eta, \pi, \psi, \bar{\sigma})}$  denote the field strength renormalization constant, while  $Z_{(m, \lambda_1, \lambda_2, g, h, c)} = 1 + \delta Z_{(m, \lambda_1, \lambda_2, g, h, c)}$  denote the mass and coupling renormalization constant.

The scalar ( $\sigma$ ,  $a_0$ ) and pseudoscalar ( $\pi$ ,  $\eta$ ) meson inverse propagators with self-energy correction are written as

$$p^2 - m_{\sigma, a_0, \pi, \eta}^2 - i\Sigma_{\sigma, a_0, \pi, \eta}(p^2) + \text{counterterms}. \quad (\text{B5})$$

Implementing the on-shell scheme, one puts the physical mass equal to the renormalized mass in the Lagrangian, i.e.,  $m = m_{\text{pole}}^1$  and writes

$$\Sigma(p^2 = m_{\sigma, a_0, \pi, \eta}^2) + \text{counterterms} = 0. \quad (\text{B6})$$

The on-shell scheme demands that the propagator residue becomes unity, and one gets

$$\frac{\partial}{\partial p^2} \Sigma_{\sigma, a_0, \pi, \eta}(p^2) \Big|_{p^2 = m_{\sigma, a_0, \pi, \eta}^2} + \text{counterterms} = 0. \quad (\text{B7})$$

The quark one-loop correction to the one-point function and the tadpole counterterm can be written as

$$\delta\Gamma^{(1)} = -4N_c g m_q \mathcal{A}(m_q^2) + i\delta t, \quad (\text{B8})$$

when the one-point function  $\Gamma^{(1)} = it = i(h - m_\pi^2 \bar{\sigma})$  vanishes, one gets the equation of motion  $t = 0$  at tree level. This should hold also at one-loop level, which results into the renormalization condition  $\delta\Gamma^{(1)} = 0$ .

The counterterms of the two-point functions are

$$\Sigma_\sigma^{\text{ct1}}(p^2) = i[\delta Z_\sigma(p^2 - m_\sigma^2) - \delta m_\sigma^2], \quad (\text{B9})$$

$$\Sigma_{a_0}^{\text{ct1}}(p^2) = i[\delta Z_{a_0}(p^2 - m_{a_0}^2) - \delta m_{a_0}^2], \quad (\text{B10})$$

$$\Sigma_\pi^{\text{ct1}}(p^2) = i[\delta Z_\pi(p^2 - m_\pi^2) - \delta m_\pi^2], \quad (\text{B11})$$

$$\Sigma_\eta^{\text{ct1}}(p^2) = i[\delta Z_\eta(p^2 - m_\eta^2) - \delta m_\eta^2], \quad (\text{B12})$$

$$\begin{aligned} \Sigma_\sigma^{\text{ct2}} &= 3\Sigma_\pi^{\text{ct2}} = 3\Sigma_\eta^{\text{ct2}}, \\ &= -\frac{24(\lambda_1 + \frac{\lambda_2}{2})g\bar{\sigma}N_c m_q}{m_\sigma^2} \mathcal{A}(m_q^2), \\ &= \frac{-6i(\lambda_1 + \frac{\lambda_2}{2})\bar{\sigma}\delta t}{m_\sigma^2}, \end{aligned} \quad (\text{B13})$$

$$\begin{aligned} \Sigma_{a_0}^{\text{ct2}} &= -\frac{8(\lambda_1 + \frac{3\lambda_2}{2})g\bar{\sigma}N_c m_q \mathcal{A}(m_q^2)}{m_\sigma^2} \\ &= -\frac{2i(\lambda_1 + \frac{3\lambda_2}{2})\bar{\sigma}\delta t}{m_\sigma^2} \end{aligned} \quad (\text{B14})$$

$$\delta t = -4iN_c g m_q \mathcal{A}(m_q^2). \quad (\text{B15})$$

The respective tadpole contributions to the  $\sigma$ ,  $a_0$ , and  $\pi$ ,  $\eta$  self-energies are canceled by the counterterms in Eq. (B13). The on-shell evaluation of the self-energies and their derivatives give all the renormalization constants. Combining the Eqs. (B6), (B7), and (B9)–(B12), one obtains the following set of equations:

$$\delta m_\sigma^2 = -i\Sigma_\sigma(m_\sigma^2); \quad \delta Z_\sigma = i \frac{\partial}{\partial p^2} \Sigma_\sigma(p^2) \Big|_{p^2 = m_\sigma^2}, \quad (\text{B16})$$

$$\delta m_{a_0}^2 = -i\Sigma_{a_0}(m_{a_0}^2); \quad \delta Z_{a_0} = i \frac{\partial}{\partial p^2} \Sigma_{a_0}(p^2) \Big|_{p^2 = m_{a_0}^2}, \quad (\text{B17})$$

$$\delta m_\pi^2 = -i\Sigma_\pi(m_\pi^2); \quad \delta Z_\pi = i \frac{\partial}{\partial p^2} \Sigma_\pi(p^2) \Big|_{p^2 = m_\pi^2}, \quad (\text{B18})$$

$$\delta m_\eta^2 = -i\Sigma_\eta(m_\eta^2); \quad \delta Z_\eta = i \frac{\partial}{\partial p^2} \Sigma_\eta(p^2) \Big|_{p^2 = m_\eta^2}. \quad (\text{B19})$$

Using the above equations and the expressions of meson self-energies given in Ref. [67], we can write

$$\delta m_\sigma^2 = 2ig^2 N_c \left[ \mathcal{A}(m_q^2) - \frac{1}{2}(m_\sigma^2 - 4m_q^2)\mathcal{B}(m_\sigma^2) \right], \quad (\text{B20})$$

$$\delta m_{a_0}^2 = 2ig^2 N_c \left[ \mathcal{A}(m_q^2) - \frac{1}{2}(m_{a_0}^2 - 4m_q^2)\mathcal{B}(m_{a_0}^2) \right], \quad (\text{B21})$$

$$\delta m_\pi^2 = 2ig^2 N_c \left[ \mathcal{A}(m_q^2) - \frac{1}{2}m_\pi^2 \mathcal{B}(m_\pi^2) \right], \quad (\text{B22})$$

$$\delta m_\eta^2 = 2ig^2 N_c \left[ \mathcal{A}(m_q^2) - \frac{1}{2}m_\eta^2 \mathcal{B}(m_\eta^2) \right], \quad (\text{B23})$$

$$\delta Z_\sigma = ig^2 N_c [\mathcal{B}(m_\sigma^2) + (m_\sigma^2 - 4m_q^2)\mathcal{B}'(m_\sigma^2)], \quad (\text{B24})$$

$$\delta Z_{a_0} = ig^2 N_c [\mathcal{B}(m_{a_0}^2) + (m_{a_0}^2 - 4m_q^2)\mathcal{B}'(m_{a_0}^2)], \quad (\text{B25})$$

$$\delta Z_\pi = ig^2 N_c [\mathcal{B}(m_\pi^2) + m_\pi^2 \mathcal{B}'(m_\pi^2)], \quad (\text{B26})$$

$$\delta Z_\eta = ig^2 N_c [\mathcal{B}(m_\eta^2) + m_\eta^2 \mathcal{B}'(m_\eta^2)], \quad (\text{B27})$$

where  $\mathcal{A}(m_q^2)$  and  $\mathcal{B}(p^2)$  are defined in the Appendix C.

The counterterms  $\delta m^2$ ,  $\delta\lambda_1$ ,  $\delta\lambda_2$ ,  $\delta c$ , and  $\delta g^2$ ,  $\delta h$  can be expressed in terms of the counterterms  $\delta m_\sigma^2$ ,  $\delta m_{a_0}^2$ ,  $\delta m_\pi^2$ ,  $\delta m_\eta^2$ , and  $\delta m_q$ ,  $\delta\bar{\sigma}^2$ . Using Eqs. (12)–(16) together with Eqs. (B1)–(B4), we can write

$$\delta\lambda_1 = \frac{\delta m_\sigma^2 + \delta m_\eta^2 - \delta m_{a_0}^2 - \delta m_\pi^2}{2\bar{\sigma}^2} - \lambda_1 \frac{\delta\bar{\sigma}^2}{\bar{\sigma}^2}, \quad (\text{B28})$$

<sup>1</sup>The imaginary parts of the self-energies are ignored for defining the mass.

$$\delta\lambda_2 = \frac{\delta m_{a_0}^2 - \delta m_\eta^2}{\bar{\sigma}^2} - \lambda_2 \frac{\delta\bar{\sigma}^2}{\bar{\sigma}^2}, \quad (\text{B29})$$

$$\delta c = \frac{\delta m_\eta^2 - \delta m_\pi^2}{2}, \quad (\text{B30})$$

$$\delta m^2 = \delta m_\pi^2 + \frac{\delta m_\eta^2 - \delta m_\sigma^2}{2}, \quad (\text{B31})$$

$$\frac{\delta g^2}{4} = \frac{\delta m_q^2}{\bar{\sigma}^2} - g^2 \frac{\delta\bar{\sigma}^2}{4\bar{\sigma}^2}. \quad (\text{B32})$$

The one loop correction at the pion-quark vertex is of order  $N_c^0$ . Hence,  $Z_\psi = 1$  and the quark self energy correction  $\delta m_q = 0$  at this order. In consequence, we get  $Z_\psi \sqrt{Z_{g^2} g^2} \sqrt{Z_\pi} \approx g(1 + \frac{1}{2} \frac{\delta g^2}{g^2} + \frac{1}{2} \delta Z_\pi) = g$ ; thus,  $\frac{\delta g^2}{g^2} + \delta Z_\pi = 0$ . Furthermore, the  $\delta m_q = 0$  implies that  $\delta g\bar{\sigma}/2 + g\delta\bar{\sigma}/2 = 0$ . Eq. (31) gives

$$\frac{\delta\bar{\sigma}^2}{\bar{\sigma}^2} = -\frac{\delta g^2}{g^2} = \delta Z_\pi. \quad (\text{B33})$$

Now we can rewrite Eqs. (B28) and (28) as

$$\delta\lambda_1 = \frac{\delta m_\sigma^2 + \delta m_\eta^2 - \delta m_{a_0}^2 - \delta m_\pi^2}{2\bar{\sigma}^2} - \lambda_1 \delta Z_\pi, \quad (\text{B34})$$

$$\delta\lambda_2 = \frac{\delta m_{a_0}^2 - \delta m_\eta^2}{\bar{\sigma}^2} - \lambda_2 \delta Z_\pi. \quad (\text{B35})$$

The equation  $h = t + m_\pi^2 \bar{\sigma}$  enables the writing of the counterterm  $\delta h$  in terms of the tadpole counterterm  $\delta t$ ,

$$\delta h = m_\pi^2 \delta\bar{\sigma} + \delta m_\pi^2 \bar{\sigma} + \delta t. \quad (\text{B36})$$

Using Eq. (B33), we can write

$$\delta t = -\frac{1}{2} m_\pi^2 \bar{\sigma} \delta Z_\pi - \delta m_\pi^2 \bar{\sigma} + \delta h. \quad (\text{B37})$$

Exploiting the Eqs. (B20)–(B27) together with the Eqs. (B28)–(B33) and (B37), we find the following expressions for the counterterms in the on-shell scheme:

$$\begin{aligned} \delta\lambda_{1\text{OS}} &= \frac{iN_c g^2}{\bar{\sigma}} \left[ -\frac{1}{2}(m_\sigma^2 - 4m_q^2)\mathcal{B}(m_\sigma^2) - \frac{1}{2}m_\eta^2\mathcal{B}(m_\eta^2) + \frac{1}{2}(m_{a_0}^2 - 4m_q^2)\mathcal{B}(m_{a_0}^2) + \frac{1}{2}m_\pi^2\mathcal{B}(m_\pi^2) \right] - \lambda_1 i g^2 N_c [\mathcal{B}(m_\pi^2) + m_\pi^2 \mathcal{B}'(m_\pi^2)] \\ &= \delta\lambda_{1\text{div}} + \frac{N_c g^2}{(4\pi)^2} \left[ 2\lambda_1 \log\left(\frac{\Lambda^2}{m_q^2}\right) + \lambda_1 (\mathcal{C}(m_\pi^2) + m_\pi^2 \mathcal{C}'(m_\pi^2)) \right. \\ &\quad \left. + \frac{(m_\sigma^2 - 4m_q^2)\mathcal{C}(m_\sigma^2) + m_\eta^2\mathcal{C}(m_\eta^2) - (m_{a_0}^2 - 4m_q^2)\mathcal{C}(m_{a_0}^2) - m_\pi^2\mathcal{C}(m_\pi^2)}{2\bar{\sigma}^2} \right], \end{aligned} \quad (\text{B38})$$

$$\begin{aligned} \delta\lambda_{2\text{OS}} &= \frac{iN_c g^2}{\bar{\sigma}^2} [-(m_{a_0}^2 - 4m_q^2)\mathcal{B}(m_{a_0}^2) + m_\eta^2\mathcal{B}(m_\eta^2)] - \lambda_2 i g^2 N_c [\mathcal{B}(m_\pi^2) + m_\pi^2 \mathcal{B}'(m_\pi^2)], \\ &= \delta\lambda_{2\text{div}} + \frac{N_c g^2}{(4\pi)^2} \left[ (2\lambda_2 - g^2) \log\left(\frac{\Lambda^2}{m_q^2}\right) + \frac{(m_{a_0}^2 - 4m_q^2)\mathcal{C}(m_{a_0}^2) - m_\eta^2\mathcal{C}(m_\eta^2)}{\bar{\sigma}^2} + \lambda_2 (m_\pi^2 \mathcal{C}'(m_\pi^2) + \mathcal{C}(m_\pi^2)) \right], \end{aligned} \quad (\text{B39})$$

$$\begin{aligned} \delta m_{\text{OS}}^2 &= 2iN_c g^2 \left[ \mathcal{A}(m_q^2) - \frac{1}{2} m_\pi^2 \mathcal{B}(m_\pi^2) \right] + iN_c g^2 \left[ -\frac{1}{2} m_\eta^2 \mathcal{B}(m_\eta^2) + \frac{1}{2} (m_\sigma^2 - 4m_q^2) \mathcal{B}(m_\sigma^2) \right] \\ &= \delta m_{\text{div}}^2 + \frac{N_c g^2}{(4\pi)^2} \left[ m^2 \log\left(\frac{\Lambda^2}{m_q^2}\right) + m_\pi^2 \mathcal{C}(m_\pi^2) + \frac{m_\eta^2 \mathcal{C}(m_\eta^2) - (m_\sigma^2 - 4m_q^2) \mathcal{C}(m_\sigma^2)}{2} - 2m_q^2 \right], \end{aligned} \quad (\text{B40})$$

$$\delta c_{\text{OS}} = \frac{iN_c g^2}{2} [-m_\eta^2 \mathcal{B}(m_\eta^2) + m_\pi^2 \mathcal{B}(m_\pi^2)] = \delta c_{\text{div}} + \frac{N_c g^2}{(4\pi)^2} \left[ c \log\left(\frac{\Lambda^2}{m_q^2}\right) + \frac{m_\eta^2 \mathcal{C}(m_\eta^2) - m_\pi^2 \mathcal{C}(m_\pi^2)}{2} \right], \quad (\text{B41})$$

$$\delta g_{\text{OS}}^2 = -iN_c g^4 [m_\pi^2 \mathcal{B}'(m_\pi^2) + \mathcal{B}(m_\pi^2)] = \delta g_{\text{div}}^2 + \frac{N_c g^4}{(4\pi)^2} \left[ \log\left(\frac{\Lambda^2}{m_q^2}\right) + \mathcal{C}(m_\pi^2) + m_\pi^2 \mathcal{C}'(m_\pi^2) \right], \quad (\text{B42})$$

$$\delta\bar{\sigma}_{\text{OS}}^2 = iN_c g^2 \bar{\sigma}^2 [m_\pi^2 \mathcal{B}'(m_\pi^2) + \mathcal{B}(m_\pi^2)] = \delta\bar{\sigma}_{\text{div}}^2 - \frac{N_c g^2 \bar{\sigma}^2}{(4\pi)^2} \left[ \log\left(\frac{\Lambda^2}{m_q^2}\right) + \mathcal{C}(m_\pi^2) + m_\pi^2 \mathcal{C}'(m_\pi^2) \right] \quad (\text{B43})$$

$$\delta h_{\text{OS}} = \frac{iN_c g^2}{2(4\pi)^2} h [m_\pi^2 \mathcal{B}'(m_\pi^2) - \mathcal{B}(m_\pi^2)] = \delta h_{\text{div}} + \frac{N_c g^2}{2(4\pi)^2} h \left[ \log\left(\frac{\Lambda^2}{m_q^2}\right) + \mathcal{C}(m_\pi^2) - m_\pi^2 \mathcal{C}'(m_\pi^2) \right] \quad (\text{B44})$$

$$\delta Z_\pi^{\text{OS}} = \delta Z_{\pi,\text{div}} - \frac{N_c g^2}{(4\pi)^2} \left[ \log\left(\frac{\Lambda^2}{m_q^2}\right) + \mathcal{C}(m_\pi^2) + m_\pi^2 \mathcal{C}'(m_\pi^2) \right]. \quad (\text{B45})$$

The  $\mathcal{B}(m^2), \mathcal{B}'(m^2)$  and  $\mathcal{C}(m^2), \mathcal{C}'(m^2)$  are defined in the Appendix. The divergent part of the counterterms are  $\delta\lambda_{1\text{div}} = \frac{N_c g^2 2\lambda_1}{(4\pi)^2 \epsilon}$ ,  $\delta\lambda_{2\text{div}} = \frac{N_c g^2}{(4\pi)^2 \epsilon} (2\lambda_2 - g^2)$ ,  $\delta m_{\text{div}}^2 = \frac{N_c g^2 m^2}{(4\pi)^2 \epsilon}$ ,  $\delta c_{\text{div}} = \frac{N_c g^2 c}{(4\pi)^2 \epsilon}$ ,  $\delta g_{\text{div}}^2 = \frac{N_c g^4}{(4\pi)^2 \epsilon}$ ,  $\delta \bar{\sigma}_{\text{div}}^2 = -\frac{N_c g^2 \bar{\sigma}^2}{(4\pi)^2 \epsilon}$ ,  $\delta h_{\text{div}} = \frac{N_c g^2 h}{2(4\pi)^2 \epsilon}$ ,  $\delta Z_{\pi, \text{div}} = -\frac{N_c g^2}{(4\pi)^2 \epsilon}$ .

For both, the on-shell and the  $\overline{\text{MS}}$  schemes, the divergent part of the counterterms are the same, i.e.,  $\delta\lambda_{1\text{div}} = \delta\lambda_{1\overline{\text{MS}}}$ ,  $\delta\lambda_{2\text{div}} = \delta\lambda_{2\overline{\text{MS}}}$  etc.

Since the bare parameters are independent of the renormalization scheme, we can immediately write down the relations between the renormalized parameters in the on-shell and MS schemes. We find

$$\lambda_{1\overline{\text{MS}}} = \frac{Z_{\lambda_1}^{\text{OS}}}{Z_{\lambda_1}^{\overline{\text{MS}}}} \lambda_1 \approx \lambda_1 + \delta\lambda_{1\text{OS}} - \delta\lambda_{1\overline{\text{MS}}}, \quad (\text{B46})$$

$$\lambda_{2\overline{\text{MS}}} = \frac{Z_{\lambda_2}^{\text{OS}}}{Z_{\lambda_2}^{\overline{\text{MS}}}} \lambda_2 \approx \lambda_2 + \delta\lambda_{2\text{OS}} - \delta\lambda_{2\overline{\text{MS}}}, \quad (\text{B47})$$

$$m_{\overline{\text{MS}}}^2 = \frac{Z_m^{\text{OS}}}{Z_m^{\overline{\text{MS}}}} m^2 \approx m^2 + \delta m_{\text{OS}}^2 - \delta m_{\overline{\text{MS}}}^2, \quad (\text{B48})$$

$$c_{\overline{\text{MS}}} = \frac{Z_c^{\text{OS}}}{Z_c^{\overline{\text{MS}}}} c \approx c + \delta c_{\text{OS}} - \delta c_{\overline{\text{MS}}}, \quad (\text{B49})$$

$$h_{\overline{\text{MS}}} = \frac{Z_h^{\text{OS}}}{Z_h^{\overline{\text{MS}}}} h \approx h + \delta h_{\text{OS}} - \delta h_{\overline{\text{MS}}}, \quad (\text{B50})$$

$$g_{\overline{\text{MS}}}^2 = \frac{Z_g^{\text{OS}}}{Z_g^{\overline{\text{MS}}}} g^2 \approx g^2 + \delta g_{\text{OS}}^2 - \delta g_{\overline{\text{MS}}}^2, \quad (\text{B51})$$

$$\bar{\sigma}_{\overline{\text{MS}}}^2 = \frac{Z_{\bar{\sigma}}^{\text{OS}}}{Z_{\bar{\sigma}}^{\overline{\text{MS}}}} \bar{\sigma}^2 \approx \bar{\sigma}^2 + \delta \bar{\sigma}_{\text{OS}}^2 - \delta \bar{\sigma}_{\overline{\text{MS}}}^2. \quad (\text{B52})$$

The minimum of the effective potential is at  $\bar{\sigma} = f_\pi$ , and masses have been measured in vacuum. Applying in Eqs. (B38)–(B44), we find the  $\Lambda$  scale dependent parameters in  $\overline{\text{MS}}$  scheme,

$$\lambda_{1\overline{\text{MS}}}(\Lambda) = \lambda_1 + \frac{N_c g^2}{(4\pi)^2} \left[ 2\lambda_1 \log\left(\frac{\Lambda^2}{m_q^2}\right) + \lambda_1 (\mathcal{C}(m_\pi^2) + m_\pi^2 \mathcal{C}'(m_\pi^2)) + \frac{(m_\sigma^2 - 4m_q^2)\mathcal{C}(m_\sigma^2) + m_\eta^2 \mathcal{C}(m_\eta^2) - (m_{a_0}^2 - 4m_q^2)\mathcal{C}(m_{a_0}^2) - m_\pi^2 \mathcal{C}(m_\pi^2)}{2f_\pi^2} \right], \quad (\text{B53})$$

$$\lambda_{2\overline{\text{MS}}}(\Lambda) = \lambda_2 + \frac{N_c g^2}{(4\pi)^2} \left[ (2\lambda_2 - g^2) \log\left(\frac{\Lambda^2}{m_q^2}\right) + \frac{(m_{a_0}^2 - 4m_q^2)\mathcal{C}(m_{a_0}^2) - m_\eta^2 \mathcal{C}(m_\eta^2)}{f_\pi^2} + \lambda_2 (\mathcal{C}(m_\pi^2) + m_\pi^2 \mathcal{C}'(m_\pi^2)) \right], \quad (\text{B54})$$

$$m_{\overline{\text{MS}}}^2(\Lambda) = m^2 + \frac{N_c g^2}{(4\pi)^2} \left[ m^2 \log\left(\frac{\Lambda^2}{m_q^2}\right) + m_\pi^2 \mathcal{C}(m_\pi^2) + \frac{m_\eta^2 \mathcal{C}(m_\eta^2) - (m_\sigma^2 - 4m_q^2)\mathcal{C}(m_\sigma^2) - 2m_q^2}{2} \right], \quad (\text{B55})$$

$$c_{\overline{\text{MS}}}(\Lambda) = c + \frac{N_c g^2}{(4\pi)^2} \left[ c \log\left(\frac{\Lambda^2}{m_q^2}\right) + \frac{m_\eta^2 \mathcal{C}(m_\eta^2) - m_\pi^2 \mathcal{C}(m_\pi^2)}{2} \right], \quad (\text{B56})$$

$$h_{\overline{\text{MS}}}(\Lambda) = h + \frac{N_c g^2}{2(4\pi)^2} h \left[ \log\left(\frac{\Lambda^2}{m_q^2}\right) + \mathcal{C}(m_\pi^2) - m_\pi^2 \mathcal{C}'(m_\pi^2) \right], \quad (\text{B57})$$

$$g_{\overline{\text{MS}}}^2(\Lambda) = g^2 + \frac{N_c g^4}{(4\pi)^2} \left[ \log\left(\frac{\Lambda^2}{m_q^2}\right) + \mathcal{C}(m_\pi^2) + m_\pi^2 \mathcal{C}'(m_\pi^2) \right], \quad (\text{B58})$$

$$\bar{\sigma}_{\overline{\text{MS}}}^2(\Lambda) = \bar{\sigma}^2 - \frac{4N_c m_q^2}{(4\pi)^2} \left[ \log\left(\frac{\Lambda^2}{m_q^2}\right) + \mathcal{C}(m_\pi^2) + m_\pi^2 \mathcal{C}'(m_\pi^2) \right], \quad (\text{B59})$$

Where the physical on-shell parameters are related with meson and quark mass values obtained in vacuum as given by Eqs. (17)–(23).

In the large- $N_c$  limit, the parameters  $\lambda_{1\overline{\text{MS}}}, \lambda_{2\overline{\text{MS}}}, m_{\overline{\text{MS}}}^2, c_{\overline{\text{MS}}}, h_{\overline{\text{MS}}}$ , and  $g_{\overline{\text{MS}}}^2$  are running with the scale  $\Lambda$  and a set of simultaneous renormalization group equations are satisfied, which are

$$\frac{d\lambda_{1\overline{\text{MS}}}(\Lambda)}{d\log(\Lambda)} = \frac{4N_c}{(4\pi)^2} g_{\overline{\text{MS}}}^2 \lambda_{1\overline{\text{MS}}}, \quad (\text{B60})$$

$$\frac{d\lambda_{2\overline{\text{MS}}}(\Lambda)}{d\log(\Lambda)} = \frac{2N_c}{(4\pi)^2} \left[ 2\lambda_{2\overline{\text{MS}}}g_{\overline{\text{MS}}}^2 - g_{\overline{\text{MS}}}^4 \right], \quad (\text{B61})$$

$$\frac{dm_{\overline{\text{MS}}}^2(\Lambda)}{d\log(\Lambda)} = \frac{2N_c}{(4\pi)^2} g_{\overline{\text{MS}}}^2 m_{\overline{\text{MS}}}^2, \quad (\text{B62})$$

$$\frac{dc_{\overline{\text{MS}}}(\Lambda)}{d\log(\Lambda)} = \frac{2N_c}{(4\pi)^2} g_{\overline{\text{MS}}}^2 c_{\overline{\text{MS}}}, \quad (\text{B63})$$

$$\frac{dh_{\overline{\text{MS}}}(\Lambda)}{d\log(\Lambda)} = \frac{N_c}{(4\pi)^2} g_{\overline{\text{MS}}}^2 h_{\overline{\text{MS}}}, \quad (\text{B64})$$

$$\frac{dg_{\overline{\text{MS}}}^2}{d\log(\Lambda)} = \frac{2N_c}{(4\pi)^2} g_{\overline{\text{MS}}}^4, \quad (\text{B65})$$

$$\frac{d\bar{\sigma}_{\overline{\text{MS}}}^2}{d\log(\Lambda)} = -\frac{2N_c}{(4\pi)^2} g_{\overline{\text{MS}}}^2 \bar{\sigma}_{\overline{\text{MS}}}^2. \quad (\text{B66})$$

The solutions of Eqs. (B60)–(B66) are

$$\lambda_{1\overline{\text{MS}}}(\Lambda) = \frac{\lambda_{10}}{\left(1 - \frac{N_c g_0^2}{(4\pi)^2} \log\left(\frac{\Lambda^2}{\Lambda_0^2}\right)\right)^2}, \quad (\text{B67})$$

$$g_{\overline{\text{MS}}}^2(\Lambda) = \frac{g_0^2}{1 - \frac{N_c g_0^2}{(4\pi)^2} \log\left(\frac{\Lambda^2}{\Lambda_0^2}\right)}, \quad (\text{B68})$$

$$\lambda_{2\overline{\text{MS}}}(\Lambda) = \frac{\lambda_{20} - \frac{N_c g_0^4}{(4\pi)^2} \log\left(\frac{\Lambda^2}{\Lambda_0^2}\right)}{\left(1 - \frac{N_c g_0^2}{(4\pi)^2} \log\left(\frac{\Lambda^2}{\Lambda_0^2}\right)\right)^2}, \quad (\text{B69})$$

$$m_{\overline{\text{MS}}}^2(\Lambda) = \frac{m_0^2}{1 - \frac{N_c g_0^2}{(4\pi)^2} \log\left(\frac{\Lambda^2}{\Lambda_0^2}\right)}, \quad (\text{B70})$$

$$c_{\overline{\text{MS}}}(\Lambda) = \frac{c_0}{1 - \frac{N_c g_0^2}{(4\pi)^2} \log\left(\frac{\Lambda^2}{\Lambda_0^2}\right)}, \quad (\text{B71})$$

$$h_{\overline{\text{MS}}}(\Lambda) = \frac{h_0}{\sqrt{1 - \frac{N_c g_0^2}{(4\pi)^2} \log\left(\frac{\Lambda^2}{\Lambda_0^2}\right)}}, \quad (\text{B72})$$

$$\bar{\sigma}^2 = f_\pi^2 \left[ 1 - \frac{N_c g_0^2}{(4\pi)^2} \log\left(\frac{\Lambda^2}{\Lambda_0^2}\right) \right], \quad (\text{B73})$$

where the parameters  $\lambda_{10}$ ,  $\lambda_{20}$ ,  $g_0^2$ ,  $m_0^2$ ,  $c_0$ , and  $h_0$ , are the  $\Lambda$  dependent parameters at the value  $\Lambda_0$ , where we consider  $\Lambda_0$  to satisfy the relation,

$$\log\left(\frac{\Lambda_0^2}{m_q^2}\right) + \mathcal{C}(m_\pi^2) + m_\pi^2 \mathcal{C}'(m_\pi^2) = 0. \quad (\text{B74})$$

## 1. Effective potential

The vacuum effective potential in the  $\overline{\text{MS}}$  scheme is given by

$$\Omega_{\text{vac}} = U(\bar{\sigma}_{\overline{\text{MS}}}) + \Omega_{\overline{\text{MS}}}^{q,\text{vac}} + \delta U(\bar{\sigma}_{\overline{\text{MS}}}), \quad (\text{B75})$$

where

$$U(\bar{\sigma}_{\overline{\text{MS}}}) = \frac{m_{\overline{\text{MS}}}^2(\Lambda)}{2} \bar{\sigma}_{\overline{\text{MS}}}^2 - \frac{c_{\overline{\text{MS}}}(\Lambda)}{2} \bar{\sigma}_{\overline{\text{MS}}}^2 + \frac{1}{4} \left( \lambda_{1\overline{\text{MS}}}(\Lambda) + \frac{\lambda_{2\overline{\text{MS}}}(\Lambda)}{2} \right) \bar{\sigma}_{\overline{\text{MS}}}^4 - h_{\overline{\text{MS}}}(\Lambda) \bar{\sigma}_{\overline{\text{MS}}},$$

$\delta U(\bar{\sigma}_{\overline{\text{MS}}}) = -\frac{N_c g_{\overline{\text{MS}}}^4 \bar{\sigma}_{\overline{\text{MS}}}^4}{8(4\pi)^2 \epsilon}$  and  $\Omega_{\overline{\text{MS}}}^{q,\text{vac}} = \frac{N_c g_{\overline{\text{MS}}}^4 \bar{\sigma}_{\overline{\text{MS}}}^4}{8(4\pi)^2} \left[ \frac{1}{\epsilon} + \frac{3}{2} + \ln\left(\frac{4\Lambda^2}{g_{\overline{\text{MS}}}^2 \bar{\sigma}_{\overline{\text{MS}}}^2}\right) \right]$  as in Ref. [67]. One can define the scale

$\Lambda$  independent parameter  $\Delta = \frac{g_{\overline{\text{MS}}} \bar{\sigma}_{\overline{\text{MS}}}}{2}$  using the Eqs. (B58) and (B59) and rewrite the vacuum effective potential in terms of it as

$$\Omega_{\text{vac}}(\Delta) = 2 \left( \frac{m_0^2}{g_0^2} - \frac{c_0}{g_0^2} \right) \Delta^2 + 4 \left( \frac{\lambda_{10}}{g_0^4} + \frac{\lambda_{20}}{2g_0^4} \right) \Delta^4 - 2 \frac{h_0}{g_0} \Delta + \frac{2N_c \Delta^4}{(4\pi)^2} \left[ \frac{3}{2} + \ln\left(\frac{\Lambda^2}{\Delta^2}\right) \right]. \quad (\text{B76})$$

Expressing the couplings and mass parameter in terms of the Yukawa coupling, pion decay constant, and physical meson masses, one can write

$$\begin{aligned} \Omega_{\text{vac}}(\Delta) &= \frac{(3m_\pi^2 - m_\sigma^2)f_\pi^2}{4} \left\{ 1 - \frac{N_c g^2}{(4\pi)^2} (\mathcal{C}(m_\pi^2) + m_\pi^2 \mathcal{C}'(m_\pi^2)) \right\} \frac{\Delta^2}{m_q^2} + \frac{N_c g^2 f_\pi^2}{2(4\pi)^2} \left\{ \frac{3m_\pi^2 \mathcal{C}(m_\pi^2) - (m_\sigma^2 - 4m_q^2) \mathcal{C}(m_\sigma^2)}{2} - 2m_q^2 \right\} \frac{\Delta^2}{m_q^2} \\ &+ \frac{(m_\sigma^2 - m_\pi^2)f_\pi^2}{8} \left\{ 1 - \frac{N_c g^2}{(4\pi)^2} (\mathcal{C}(m_\pi^2) + m_\pi^2 \mathcal{C}'(m_\pi^2)) \right\} \frac{\Delta^4}{m_q^4} + \frac{N_c g^2 f_\pi^2}{(4\pi)^2} \left[ \frac{(m_\sigma^2 - 4m_q^2) \mathcal{C}(m_\sigma^2) - m_\pi^2 \mathcal{C}(m_\pi^2)}{8} \right] \frac{\Delta^4}{m_q^4} \\ &+ \frac{2N_c \Delta^4}{(4\pi)^2} \left\{ \frac{3}{2} - \ln\left(\frac{\Delta^2}{m_q^2}\right) \right\} - m_\pi^2 f_\pi^2 \left\{ 1 - \frac{N_c g^2}{(4\pi)^2} m_\pi^2 \mathcal{C}'(m_\pi^2) \right\} \frac{\Delta}{m_q}. \end{aligned} \quad (\text{B77})$$

Here, it is relevant to remind ourselves that the Yukawa coupling and the pion decay constant both get renormalized in the vacuum due to the dressing of the meson propagator in the RQM model. However, the Eq. (B58) gives  $g_{\overline{\text{MS}}} = g_{\text{ren}} = g$ , and the Eq. (B59) gives  $\bar{\sigma}_{\overline{\text{MS}}} = f_{\pi, \text{ren}} = f_{\pi}$  at the scale  $\Lambda_0$ . Applying the stationarity condition  $\frac{\partial \Omega_{\text{vac}}(\Delta)}{\partial \Delta}$  to the Eq. (B76), one gets  $h_0 = m_{\pi, c}^2 \bar{\sigma}_{\overline{\text{MS}}} = m_{\pi}^2 \left\{ 1 - \frac{N_c g^2}{(4\pi)^2} m_{\pi}^2 C'(m_{\pi}^2) \right\} f_{\pi}$ . Note that the pion curvature mass  $m_{\pi, c}$  differs from its pole mass  $m_{\pi}$  on account of the consistent parameter fixing, and we have  $m_{\pi, c}^2 = m_{\pi}^2 \left\{ 1 - \frac{N_c g^2}{(4\pi)^2} m_{\pi}^2 C'(m_{\pi}^2) \right\}$  as in Ref. [63]. The minimum of the vacuum effective potential lies at  $\bar{\sigma}_{\overline{\text{MS}}} = f_{\pi}$ .

### APPENDIX C: INTEGRALS

The divergent loop integrals are regularized by incorporating dimensional regularization,

$$\int_p = \left( \frac{e^{\gamma_E} \Lambda^2}{4\pi} \right)^\epsilon \int \frac{d^d p}{(2\pi)^d}, \quad (\text{C1})$$

where  $d = 4 - 2\epsilon$ ,  $\gamma_E$  is the Euler-Mascheroni constant, and  $\Lambda$  is renormalization scale associated with the  $\overline{\text{MS}}$ .

$$\begin{aligned} \mathcal{A}(m_q^2) &= \int_p \frac{1}{p^2 - m_q^2} \\ &= \frac{im_q^2}{(4\pi)^2} \left[ \frac{1}{\epsilon} + 1 + \log(4\pi e^{-\gamma_E}) + \log\left(\frac{\Lambda^2}{m_q^2}\right) \right], \end{aligned}$$

we rewrite this after redefining  $\Lambda^2 \rightarrow \Lambda^2 \frac{e^{\gamma_E}}{4\pi}$ ,

$$\mathcal{A}(m_q^2) = \frac{im_q^2}{(4\pi)^2} \left[ \frac{1}{\epsilon} + 1 + \log\left(\frac{\Lambda^2}{m_q^2}\right) \right] \quad (\text{C2})$$

$$\begin{aligned} \mathcal{B}(p^2) &= \int_k \frac{1}{(k^2 - m_q^2)[(k+p)^2 - m_q^2]} \\ &= \frac{i}{(4\pi)^2} \left[ \frac{1}{\epsilon} + \log\left(\frac{\Lambda^2}{m_q^2}\right) + C(p^2) \right] \quad (\text{C3}) \end{aligned}$$

$$\mathcal{B}'(p^2) = \frac{i}{(4\pi)^2} C'(p^2). \quad (\text{C4})$$

$$\begin{aligned} \mathcal{C}(p^2) &= 2 - 2\sqrt{\frac{4m_q^2}{p^2} - 1} \arctan\left(\frac{1}{\sqrt{\frac{4m_q^2}{p^2} - 1}}\right); \\ \mathcal{C}'(p^2) &= \frac{4m_q^2}{p^4 \sqrt{\frac{4m_q^2}{p^2} - 1}} \arctan\left(\frac{1}{\sqrt{\frac{4m_q^2}{p^2} - 1}}\right) - \frac{1}{p^2}, \quad (\text{C5}) \end{aligned}$$

$$\begin{aligned} \mathcal{C}(p^2) &= 2 + \sqrt{1 - \frac{4m_q^2}{p^2}} \ln\left(\frac{1 - \sqrt{1 - \frac{4m_q^2}{p^2}}}{1 + \sqrt{1 - \frac{4m_q^2}{p^2}}}\right); \\ \mathcal{C}'(p^2) &= \frac{2m_q^2}{p^4 \sqrt{\frac{4m_q^2}{p^2} - 1}} \ln\left(\frac{1 - \sqrt{1 - \frac{4m_q^2}{p^2}}}{1 + \sqrt{1 - \frac{4m_q^2}{p^2}}}\right) - \frac{1}{p^2}, \quad (\text{C6}) \end{aligned}$$

The Eqs. (C5) and (C6) are valid with the constraints ( $p^2 < 4m_q^2$ ) and ( $p^2 > 4m_q^2$ ), respectively.

- 
- [1] N. Cabibbo and G. Parisi, *Phys. Lett.* **59B**, 67 (1975).  
[2] L. D. McLerran and B. Svetitsky, *Phys. Rev. D* **24**, 450 (1981); B. Svetitsky, *Phys. Rep.* **132**, 1 (1986).  
[3] B. Muller, *Rep. Prog. Phys.* **58**, 611 (1995).  
[4] H. Meyer-Ortmanns, *Rev. Mod. Phys.* **68**, 473 (1996).  
[5] D. H. Rischke, *Prog. Part. Nucl. Phys.* **52**, 197 (2004).  
[6] A. Ali Khan *et al.*, *Phys. Rev. D* **64**, 074510 (2001).  
[7] S. Digoal, E. Laermann, and H. Satz, *Eur. Phys. J. C* **18**, 583 (2001).  
[8] F. Karsch, *Lect. Notes Phys.* **583**, 209 (2002).  
[9] Z. Fodor, S. D. Katz, and K. K. Szabo, *Phys. Lett. B* **568**, 73 (2003).  
[10] C. R. Allton, M. Doring, S. Ejiri, S. J. Hands, O. Kaczmarek, F. Karsch, E. Laermann, and K. Redlich, *Phys. Rev. D* **71**, 054508 (2005).  
[11] F. Karsch, *J. Phys. G* **31**, S633 (2005).  
[12] Y. Aoki, Z. Fodor, S. D. Katz, and K. K. Szabo, *Phys. Lett. B* **643**, 46 (2006).  
[13] M. Cheng *et al.*, *Phys. Rev. D* **74**, 054507 (2006).  
[14] M. Cheng *et al.*, *Phys. Rev. D* **77**, 014511 (2008).  
[15] J. Langelage, S. Lottini, and O. Philipsen, *J. High Energy Phys.* **02** (2011) 057.  
[16] M. G. Alford, A. Schmitt, and K. Rajagopal, *Rev. Mod. Phys.* **80**, 1455 (2008).  
[17] G. Fejos, *Phys. Rev. D* **92**, 036011 (2015).  
[18] G. Fejos and A. Hosaka, *Phys. Rev. D* **94**, 036005 (2016).  
[19] G. Fejos and A. Hosaka, *Phys. Rev. D* **98**, 036009 (2018).  
[20] G. Fejos and A. Patkos, *Phys. Rev. D* **105**, 096007 (2022).  
[21] K. Fukushima and T. Hatsuda, *Rep. Prog. Phys.* **74**, 014001 (2011).

- [22] D. Roder, J. Ruppert, and D. H. Rischke, *Phys. Rev. D* **68**, 016003 (2003).
- [23] K. Fukushima, K. Kamikado, and B. Klein, *Phys. Rev. D* **83**, 116005 (2011).
- [24] M. Grahl and D. H. Rischke, *Phys. Rev. D* **88**, 056014 (2013).
- [25] J. T. Lenaghan, D. H. Rischke, and J. Schaffner-Bielich, *Phys. Rev. D* **62**, 085008 (2000); J. T. Lenaghan and D. H. Rischke, *J. Phys. G* **26**, 431 (2000).
- [26] A. Jakovac, A. Patkos, Z. Szep, and P. Szeplfalusy, *Phys. Lett. B* **582**, 179 (2004).
- [27] T. Herpay, A. Patkós, Zs. Szép, and P. Szeplfalusy, *Phys. Rev. D* **71**, 125017 (2005).
- [28] T. Herpay and Zs. Szép, *Phys. Rev. D* **74**, 025008 (2006).
- [29] P. Kovács and Zs. Szép, *Phys. Rev. D* **75**, 025015 (2007).
- [30] P. Kovacs and Zs. Szep, *Phys. Rev. D* **75**, 025015 (2007).
- [31] T. Kahara and K. Tuominen, *Phys. Rev. D* **78**, 034015 (2008); **80**, 114022 (2009); **82**, 114026 (2010).
- [32] E. S. Bowman and J. I. Kapusta, *Phys. Rev. C* **79**, 015202 (2009); J. I. Kapusta and E. S. Bowman, *Nucl. Phys. A* **830**, 721C (2009).
- [33] G. Fejos and A. Patkos, *Phys. Rev. D* **82**, 045011 (2010).
- [34] A. Jakovac and Zs. Szep, *Phys. Rev. D* **82**, 125038 (2010).
- [35] L. Ferroni, V. Koch, and M. B. Pinto, *Phys. Rev. C* **82**, 055205 (2010).
- [36] G. Marko and Zs. Szep, *Phys. Rev. D* **82**, 065021 (2010).
- [37] O. Scavenuius, A. Mocsy, I. N. Mishustin, and D. H. Rischke, *Phys. Rev. C* **64**, 045202 (2001).
- [38] A. Mocsy, I. N. Mishustin, and P. J. Ellis, *Phys. Rev. C* **70**, 015204 (2004).
- [39] B.-J. Schaefer and J. Wambach, *Nucl. Phys. A* **757**, 479 (2005).
- [40] B.-J. Schaefer and J. Wambach, *Phys. Rev. D* **75**, 085015 (2007).
- [41] B. J. Schaefer and M. Wagner, *Phys. Rev. D* **79**, 014018 (2009).
- [42] R. D. Pisarski and F. Wilczek, *Phys. Rev. D* **29**, 338 (1984).
- [43] A. Halasz, A. D. Jackson, R. E. Shrock, M. A. Stephanov, and J. J. M. Verbaarschot, *Phys. Rev. D* **58**, 096007 (1998).
- [44] V. Skokov, B. Friman, E. Nakano, K. Redlich, and B.-J. Schaefer, *Phys. Rev. D* **82**, 034029 (2010).
- [45] R. Khan and L. T. Kyllingstad, *AIP Conf. Proc.* **1343**, 504 (2011).
- [46] U. S. Gupta and V. K. Tiwari, *Phys. Rev. D* **85**, 014010 (2012).
- [47] B.-J. Schaefer and M. Wagner, *Phys. Rev. D* **85**, 034027 (2012).
- [48] S. Chatterjee and K. A. Mohan, *Phys. Rev. D* **85**, 074018 (2012).
- [49] J. O. Andersen and A. Tranberg, *J. High Energy Phys.* **08** (2012) 002.
- [50] V. K. Tiwari, *Phys. Rev. D* **86**, 094032 (2012).
- [51] S. Chatterjee and K. A. Mohan, *Phys. Rev. D* **86**, 114021 (2012).
- [52] V. K. Tiwari, *Phys. Rev. D* **88**, 074017 (2013).
- [53] T. K. Herbst, J. M. Pawlowski, and B.-J. Schaefer, *Phys. Rev. D* **88**, 014007 (2013).
- [54] J. Weyrich, N. Strodthoff, and L. von Smekal, *Phys. Rev. C* **92**, 015214 (2015).
- [55] P. Kovács, Zs Szép, and Gy Wolf, *Phys. Rev. D* **93**, 114014 (2016).
- [56] Andreas Zacchi and Jürgen Schaffner-Bielich, *Phys. Rev. D* **97**, 074011 (2018).
- [57] Andreas Zacchi and Jürgen Schaffner-Bielich, *Phys. Rev. D* **100**, 123024 (2019).
- [58] S. K. Rai and V. K. Tiwari, *Eur. Phys. J. Plus* **135**, 844 (2020).
- [59] K. Kajantie, M. Laine, K. Rummukainen, and M. E. Shaposhnikov, *Nucl. Phys.* **B458**, 90 (1996).
- [60] P. Adhikari, J. O. Andersen, and P. Kneschke, *Phys. Rev. D* **95**, 036017 (2017).
- [61] S. Carignano, M. Buballa, and B.-J. Schaefer, *Phys. Rev. D* **90**, 014033 (2014).
- [62] J. O. Andersen, W. R. Naylor, and A. Tranberg, *Rev. Mod. Phys.* **88**, 025001 (2016).
- [63] S. Carignano, M. Buballa, and W. Elkamhawy, *Phys. Rev. D* **94**, 034023 (2016).
- [64] P. Adhikari, J. O. Andersen, and P. Kneschke, *Phys. Rev. D* **96**, 016013 (2017).
- [65] P. Adhikari, J. O. Andersen, and P. Kneschke, *Phys. Rev. D* **98**, 074016 (2018).
- [66] A. Folkestad and J. O. Andersen, *Phys. Rev. D* **99**, 054006 (2019).
- [67] S. K. Rai and V. K. Tiwari, *Phys. Rev. D* **105**, 094010 (2022).
- [68] A. M. Polyakov, *Phys. Lett.* **72B**, 477 (1978).
- [69] B. Svetitsky and L. G. Yaffe, *Nucl. Phys.* **B210**, 423 (1982).
- [70] T. Banks and A. Ukawa, *Nucl. Phys.* **B225**, 145 (1983).
- [71] R. D. Pisarski, *Phys. Rev. D* **62**, 111501(R) (2000).
- [72] K. Fukushima, *Phys. Lett. B* **591**, 277 (2004).
- [73] B. Layek, A. P. Mishra, A. M. Srivastava, and V. K. Tiwari, *Phys. Rev. D* **73**, 103514 (2006).
- [74] C. Ratti, M. A. Thaler, and W. Weise, *Phys. Rev. D* **73**, 014019 (2006).
- [75] S. Roessner, C. Ratti, and W. Weise, *Phys. Rev. D* **75**, 034007 (2007).
- [76] K. Fukushima, *Phys. Rev. D* **78**, 114019 (2008).
- [77] B. J. Schaefer, J. M. Pawlowski, and J. Wambach, *Phys. Rev. D* **76**, 074023 (2007).
- [78] B. J. Schaefer, M. Wagner, and J. Wambach, *Phys. Rev. D* **81**, 074013 (2010).
- [79] H. Mao, J. Jin, and M. Huang, *J. Phys. G* **37**, 035001.
- [80] U. S. Gupta and V. K. Tiwari, *Phys. Rev. D* **81**, 054019 (2010).
- [81] L. M. Haas, R. Stiele, J. Braun, J. M. Pawlowski, and J. Schaffner-Bielich, *Phys. Rev. D* **87**, 076004 (2013).
- [82] P. M. Lo, B. Friman, O. Kaczmarek, K. Redlich, and C. Sasaki, *Phys. Rev. D* **88**, 074502 (2013).
- [83] T. K. Herbst, M. Mitter, J. M. Pawlowski, B.-J. Schaefer, and R. Stiele, *Phys. Lett. B* **731**, 248 (2014).
- [84] R. Stiele and J. Schaffner-Bielich, *Phys. Rev. D* **93**, 094014 (2016).
- [85] T. K. Herbst, J. M. Pawlowski, and B.-J. Schaefer, *Phys. Lett. B* **696**, 58 (2011).
- [86] R. Kobes, G. Kunstatter, and A. Rebhan, *Phys. Rev. Lett.* **64**, 2992 (1990); *Nucl. Phys.* **B355**, 1 (1991).

- [87] A. K. Rebhan, *Phys. Rev. D* **48**, R3967 (1993).
- [88] O. Kaczmarek and F. Zantow, *Phys. Rev. D* **71**, 114510 (2005).
- [89] S. Borsányi, Z. Fodor, C. Hoelbling, S. D. Katz, S. Krieg, C. Ratti, and K. K. Szabó, *J. High Energy Phys.* **09** (2010) 73.
- [90] L. McLerran and R. D. Pisarski, *Nucl. Phys.* **A796**, 83 (2007).
- [91] L. McLerran, *Nucl. Phys.* **A830**, 709c (2009).
- [92] M. Dutra, O. Lourenço, A. Delfino, T. Frederico, and M. Malheiro, *Phys. Rev. D* **88**, 114013 (2013).
- [93] B. Mohanty and J.-E. Alam, *Phys. Rev. C* **68**, 064903 (2003).
- [94] V. K. Tiwari, *Phys. Rev. D* **108**, 074002 (2023).